

# Endosomal trafficking participates in lipid droplet catabolism to maintain lipid homeostasis

Received: 9 January 2024

Accepted: 7 February 2025

Published online: 24 February 2025



Wang Peng<sup>1,2,3,4,10</sup>, Shu Chen<sup>1,5,10</sup>, Jingyu Ma<sup>4</sup>, Wenjie Wei<sup>6</sup>, Naixin Lin<sup>1,2</sup>, Jinchao Xing<sup>1,2</sup>, Wenjing Guo<sup>7</sup>, Heying Li<sup>7</sup>, Liang Zhang<sup>1,2</sup>, Kuiming Chan<sup>1,2</sup>, Andrew Yen<sup>3</sup>, Guangyu Zhu<sup>1,5</sup>✉ & Jianbo Yue<sup>1,4,8,9</sup>✉

The interplay between lipid droplets (LDs) and endosomes remains unknown. Here, we screen and synthesize AP1-coumarin, an LD-specific probe, by conjugating a fluorescent dye coumarin to a triazine compound AP1. AP1-coumarin labels all stages of LDs in live cells and markedly induces the accumulation of enlarged RAB5-RAB7 double-positive intermediate endosomes. The AP1-coumarin-labeled LDs contact these intermediate endosomes, with some LDs even being engulfed in them. When LD biogenesis is inhibited, the ability of AP1-coumarin to label LDs is markedly reduced, and the accumulation of enlarged intermediate endosomes is abolished. Moreover, blocking the biogenesis of LDs decreases the number of late endosomes while increasing the number of early endosomes and inhibits the endosomal trafficking of low-density lipoprotein (LDL) and transferrin. Correspondingly, interference with RAB5 or RAB7, either through knockdown or using dominant-negative mutants, inhibits LD catabolism, whereas the expression of a RAB7 constitutively active mutant accelerates LD catabolism. Additionally, CCZ1 knockdown not only induces the accumulation of intermediate endosomes but also inhibits LD catabolism. These results collectively suggest that LDs and endosomes interact and influence each other's functions, and endosomal trafficking participates in the catabolic process of LDs to maintain lipid homeostasis.

Lipid droplets (LDs), also called lipid bodies or fat droplets, are cellular organelles that play an important role in the storage, metabolism, and regulation of lipids within cells. LDs are essential components of virtually all eukaryotic cells, ranging from simple single-celled organisms

to complex multicellular organisms like humans. LDs are dynamic structures composed primarily of neutral lipids, such as triglycerides and cholesterol esters, enclosed within a phospholipid monolayer. They are recognized as dynamic hubs involved in various cellular

<sup>1</sup>City University of Hong Kong Shenzhen Research Institute, Shenzhen, China. <sup>2</sup>Department of Biomedical Sciences, City University of Hong Kong, Hong Kong, China. <sup>3</sup>Department of Biomedical Sciences, Cornell University, Ithaca, NY, USA. <sup>4</sup>Division of Natural and Applied Sciences, Syner Molecular Biology Lab, Jiangsu Provincial University Key (Construction) Laboratory for Smart Diagnosis and Treatment of Lung Cancer, Duke Kunshan University, Kunshan, China. <sup>5</sup>Department of Chemistry, City University of Hong Kong, Hong Kong, China. <sup>6</sup>Core Research Facilities, Southern University of Science and Technology, Shenzhen, China. <sup>7</sup>Analysis and Testing Center, Guangzhou Institute of Biomedicine and Health (GIBH) Chinese Academy of Sciences, Guangzhou, China. <sup>8</sup>College of Life Sciences, Wuhan University, Wuhan, China. <sup>9</sup>Key Laboratory of Immune Microenvironment and Inflammatory Disease Research in Universities of Shandong Province, School of Basic Medical Sciences, Shandong Second Medical University, Weifang, China. <sup>10</sup>These authors contributed equally: Wang Peng, Shu Chen. ✉ e-mail: [guangzhu@cityu.edu.hk](mailto:guangzhu@cityu.edu.hk); [jianbo.yue@dukekunshan.edu.cn](mailto:jianbo.yue@dukekunshan.edu.cn)

processes, e.g., energy homeostasis, lipid metabolism, cellular signaling, and even roles in immunity<sup>1–3</sup>. LDs are not isolated entities but are integrated into the cellular network through contact with multiple organelles, e.g., ER, mitochondria, peroxisomes, lysosomes, autophagosomes, etc. These interactions allow LDs to play diverse roles in cellular metabolism, signaling, and homeostasis<sup>4–7</sup>.

Endosomal trafficking is a fundamental cellular process that controls the movement and sorting of various molecules within the cell. It begins with the internalization of various molecules, such as cell surface receptors and extracellular materials, into early endosomes through endocytosis. These early endosomes act as sorting hubs, where cargo is assessed and sorted based on its fate within the cell. Subsequently, cargo can be directed to different pathways: some may be recycled back to the cell surface, while others are transported to late endosomes and ultimately to lysosomes for degradation. This dynamic sorting process is crucial for maintaining cellular homeostasis, regulating signaling pathways, and managing the turnover of cellular components<sup>8–10</sup>. Endosomal maturation and trafficking involve the RAB family of GTPases where replacement of RAB5 with RAB7 facilitates conversion from early to late endosomes. Dysregulation of this process is implicated in various diseases, including neurodegenerative disorders, infectious diseases, and cancer<sup>11</sup>.

The main interaction points between LDs and degradative vesicles, such as lysosomes and autophagosomes, are believed to control LD catabolism<sup>4,5,12</sup>. However, the interaction of LDs with endosomes and their mutual dynamics remains largely unexplored. In this study, we developed a fluorescent triazine compound to investigate the relationship between endosomes and LDs. By applying this fluorescent triazine probe, we demonstrated that LDs and endosomes interact and influence each other's functions. Furthermore, endosomal trafficking plays a crucial role in the catabolic process of LDs, contributing to the maintenance of lipid homeostasis.

## Results

### A fluorophore-conjugated triazine compound specifically labels LDs in live cells

The contacts between LDs and endosomes remain largely unexplored, although several RABs were found in isolated LDs by proteomics studies<sup>13–18</sup>. We, therefore, assessed the potential contacts between LDs and endosomes by quantifying the colocalization of LDs' markers or dyes with those of endosomes. We applied Bodipy<sup>19</sup> or Nile Red<sup>20</sup>, or expressed adipose differentiation-related protein (ADRP)<sup>21</sup> or acyl-CoA synthetase 3 (ACSL3)-GFP<sup>22</sup> to label LDs in A549 cells. We also expressed GFP- or mCherry-RAB5 or RAB7 to label the earlier or late endosomes, respectively. We detected the weak colocalization between ADRP puncta and RAB5 or RAB7 puncta (Supplementary Fig. 1A). Likewise, we saw limited colocalizations of ACSL3, Bodipy, or Nile Red puncta with RAB5 or RAB7 puncta (Supplementary Fig. 1B–D). The apparent low colocalization between LDs and endosome markers may be an artifact of the imaging process. Yet, given the highly dynamic nature of endocytic vesicles and LDs, transient interactions between these organelles could account for the suboptimal colocalization of their respective markers or fluorescent dyes.

We speculated that if a compound is routed to endosomes via LDs to modulate endosomal trafficking, its fluorescent conjugate could enable real-time tracking of the interaction between LDs and endosomes. Therefore, we selected a panel of compounds known to modulate endosomal trafficking, treated A549 cells with these compounds, and isolated LDs (Supplementary Fig. 2A). The isolated LDs were then subjected to immunoblot analysis using antibodies against LD markers such as ADRP and ACSL3, mitochondria markers such as TGN46 and GM130, and cytosolic markers such as HSP70,  $\alpha$ -Tubulin and Actin. Our results demonstrated that the isolated LDs were devoid of mitochondria (Supplementary Fig. 2B). Subsequently, we performed mass spectrometry analysis on the isolated LDs to identify the presence of

these compounds within them. Interestingly, we identified API, a triazine compound we synthesized, in isolated LDs (Supplementary Fig. 2C). Therefore, we synthesized the coumarin-conjugated API, named API-Coumarin (API-C) (Supplementary Fig. 3A), and confirmed its structure via LC-MS and NMR analyses (Supplementary Fig. 3B). Like API, API-C induced large vacuoles (Supplementary Fig. 3C) and inhibited endosomal trafficking (Supplementary Fig. 3D). These results suggest that API-C or API, like its other triazine analogs<sup>23–26</sup>, is an endosomal trafficking inhibitor.

Next, we characterized the ability of API-C to label LDs in live cells. We showed that coumarin failed to stain the live cells because it is cell impermeable (Fig. 1A). Of note, even in fixed cells permeabilized with or without Tween 20 and Triton X-100, coumarin did not stain LDs (Supplementary Fig. 4A–C). Whereas API-C is cell-permeable, and API-C puncta almost completely colocalized with various LDs markers, such as Nile Red, Bodipy, mCherry-ACSL3, GFP-ADPR, mc-HSD17B11<sup>27</sup>, GFP-LiveDrop<sup>28</sup>, and LipidTox (Fig. 1B–F, and Supplementary Fig. 4D, E). We further treated live cells co-expressing GFP-ADPR and mCherry-ACSL3 with API-C for 1 h or 6 h, followed by confocal imaging. Interestingly, after 1 h treatment, some API-C/mCherry-ACSL3 double-positive puncta were ADPR-GFP negative (top panel of Fig. 1G), whereas, by 6 h treatment, API-C colocalized with both ADPR and ACSL3 on enlarged vacuoles (bottom panel of Fig. 1G). Since ADPR is a marker of matured LDs while ACSL3 is a marker of both emerging and matured LDs<sup>22,29,30</sup>, these results suggest that API-C could label LDs of all stages in live cells.

We then analyzed the stability of API-C in buffers with various pH and showed that no degradation of API-C and the fluorescence intensity of API-C is not quenched by acidic pH (Supplementary Fig. 5A–F). We also treated A549 cells with API-C for 6 h or 24 h, and the cell lysates were then subjected to LC-MS analysis. The API-C was exclusively identified at its molecular mass peak of 916.3344, confirming its presence. Conversely, no signal was detected at the mass peak corresponding to coumarin (Supplementary Fig. 5G). These results suggest that API-C is stable in cells even after 24 h incubation. We further treated API-C-labeled cells with thapsigargin (TG), a potent inhibitor of the sarco/endoplasmic reticulum  $\text{Ca}^{2+}$ -ATPase (SERCA) pump, which increases intracellular calcium levels by preventing calcium reuptake into the endoplasmic reticulum<sup>31</sup>, or  $\text{NH}_4\text{Cl}$ , a weak base that effectively raises cytosolic pH<sup>32</sup>, for 6 h or overnight. We showed that the fluorescence intensity and stability of API-C in cells were not significantly affected by the changes in  $\text{Ca}^{2+}$  or pH induced by TG or  $\text{NH}_4\text{Cl}$ , respectively (Supplementary Fig. 5H–K). In summary, these results indicate that API-C is stable both in vivo and in vitro, unaffected by pH or  $\text{Ca}^{2+}$  changes. In addition, we showed that API-C, like API, at concentrations up to 10  $\mu\text{M}$  exhibited little cytotoxicity (Supplementary Fig. 5L, M). These results suggest that API-C is a stable and non-toxic biosensor for LDs in live cells.

### Contacts between LDs and intermediate endosomes

Next, we assessed the contacts between LDs and endosomes by incubating GFP-RAB5/mCherry-RAB7-coexpressing A549 cells treated with API-C or coumarin for various times, followed by confocal imaging. As expected, coumarin failed to stain live cells, and RAB5 exhibited little colocalization with RAB7 in these cells (Fig. 2A). On the other hand, API-C treatment of live cells markedly induced the colocalization of API-C puncta with both RAB5 and RAB7 puncta in a time-dependent manner. By 3 h or 6 h after API-C treatment, some API-C puncta were apparently engulfed into endosomes (Fig. 2B). N-SIM S Super-resolution imaging was further performed on GFP-RAB7/mCherry-RAB5-coexpressing A549 cells treated with API-C. Consistently, the API-C puncta showed strong colocalization with RAB5/RAB7-double positive endosomes, and some API-C puncta appeared inside enlarged endosomes (Fig. 2C). In addition to A549 cells, clear contacts between LDs and endosomes in API-C-treated

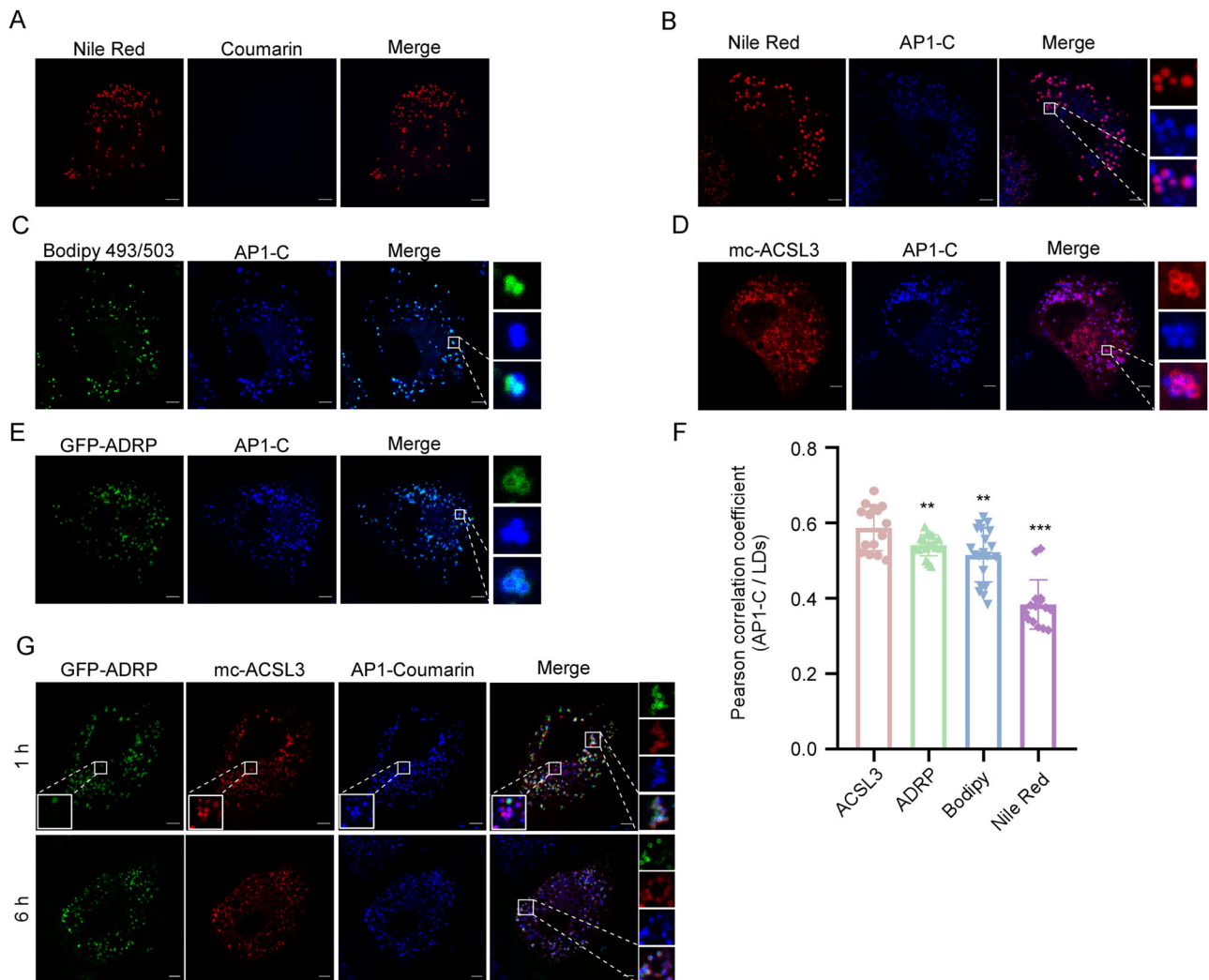


**Fig. 1 | AP1-C stains LDs of all stages in live cells.** **A–C** Live A549 cells were co-stained with Nile Red (1  $\mu$ M) and coumarin (10  $\mu$ M) (**A**) or AP1-C (10  $\mu$ M) (**B**), or Bodipy 493/503 (1  $\mu$ M) and AP1-C (10  $\mu$ M) (**C**) for 1 h, followed by confocal imaging. **D, E** A549 cells were transiently transfected with mc-ACSL3 (**D**) or GFP-ADRP (**E**), then treated with AP1-C (10  $\mu$ M) for 1 h, followed by confocal imaging. **F** Pearson correlation coefficient analysis of images in (**B–E**) was calculated by Zen black software ( $n = 15$  for Nile Red,  $n = 20$  for Bodipy 493/503,  $n = 15$  for ACSL3, and  $n = 15$  for ADRP; compared to the ACSL3 group,  $p = 0.0069$  and  $p = 0.0034$  for

ADRP and Bodipy, respectively;  $p < 0.0001$  for Nile Red). **G** A549 cells were transiently co-transfected with mc-ACSL3 and GFP-ADRP ( $n = 11$ ), then treated with AP1-C (10  $\mu$ M) for 1 h or 6 h, followed by confocal imaging. Images were finally captured by a Zeiss 880 microscope with a 63x objective lens. The scale bar is 5  $\mu$ m. The graphs represented data from three independent experiments. The statistical significance of differences was determined by using the unpaired two-tailed student's *t* test, and data quantifications were expressed as mean  $\pm$  s.e.m. \* $p < 0.05$ , \*\* $p < 0.01$ , \*\*\* $p < 0.001$ ; ns: no significance.

HepG2 and HeLa cells were observed (Supplementary Fig. 6A, B). Transmission electron microscopy (TEM) images of cells treated with AP1-C confirmed that LDs contacted and were engulfed by large endosomes (enlarged vacuoles) in AP1-C treated cells (Supplementary Fig. 6C). The LDs in AP1-C treated cells in TEM images were identified by a correlative light electron microscopy (CLEM) approach<sup>33–35</sup>. Similarly, confocal imaging combined with bright-field microscopy of AP1-C-treated A549 cells expressing mCherry-Rab7 and GFP-LiveDrop clearly showed instances of LDs contacting and being engulfed by enlarged endosomes (Supplementary Fig. 6D). Amino acid starvation is known to induce LDs biogenesis<sup>36,37</sup> and endosomal trafficking<sup>38</sup>. As expected, amino acid starvation led to a significant increase in the colocalization of Bodipy-positive LDs with Rab5-positive early endosomes and Rab7-positive late endosomes, as well as an increase in the number of LDs in contact with endosomes, compared to control cells (Supplementary Fig. 6E, F). These results support that LDs contact with endosomes.

Similar to other triazine analogs, e.g., 6J1 and V1<sup>23–26</sup>, AP1-C gradually induced the enlarged endosomes over time. To our surprise, these enlarged endosomes are RAB5 and RAB7 double-positive (Fig. 2B, C, and Supplementary Fig. 7A). We suspect that these enlarged endosomes induced by these triazine compounds are the intermediate endosomes between early- and late-endosomes. We thus treated A549 cells coexpressing GFP-RAB5 and mCherry-RAB7 with AP1, and showed that AP1 treatment significantly induced the colocalization between RAB5 and RAB7 (Supplementary Fig. 7B). We also treated cells with AP1, fixed them, and immunostained these cells with antibodies against RAB5 or RAB7. Consistently, the enlarged endosomes induced by AP1 are RAB5- and RAB7-double positive (Supplementary Fig. 7C). We further performed immunoprecipitation experiments to assess whether AP1 induces the interaction between RAB5 and RAB7. We showed that in control cells coexpressing twinstrep-RAB7 and Myc-RAB5, streptavidin beads mainly pulled down RAB7, not RAB5, whereas, in AP1-treated cells, it brought down both RAB7 and RAB5



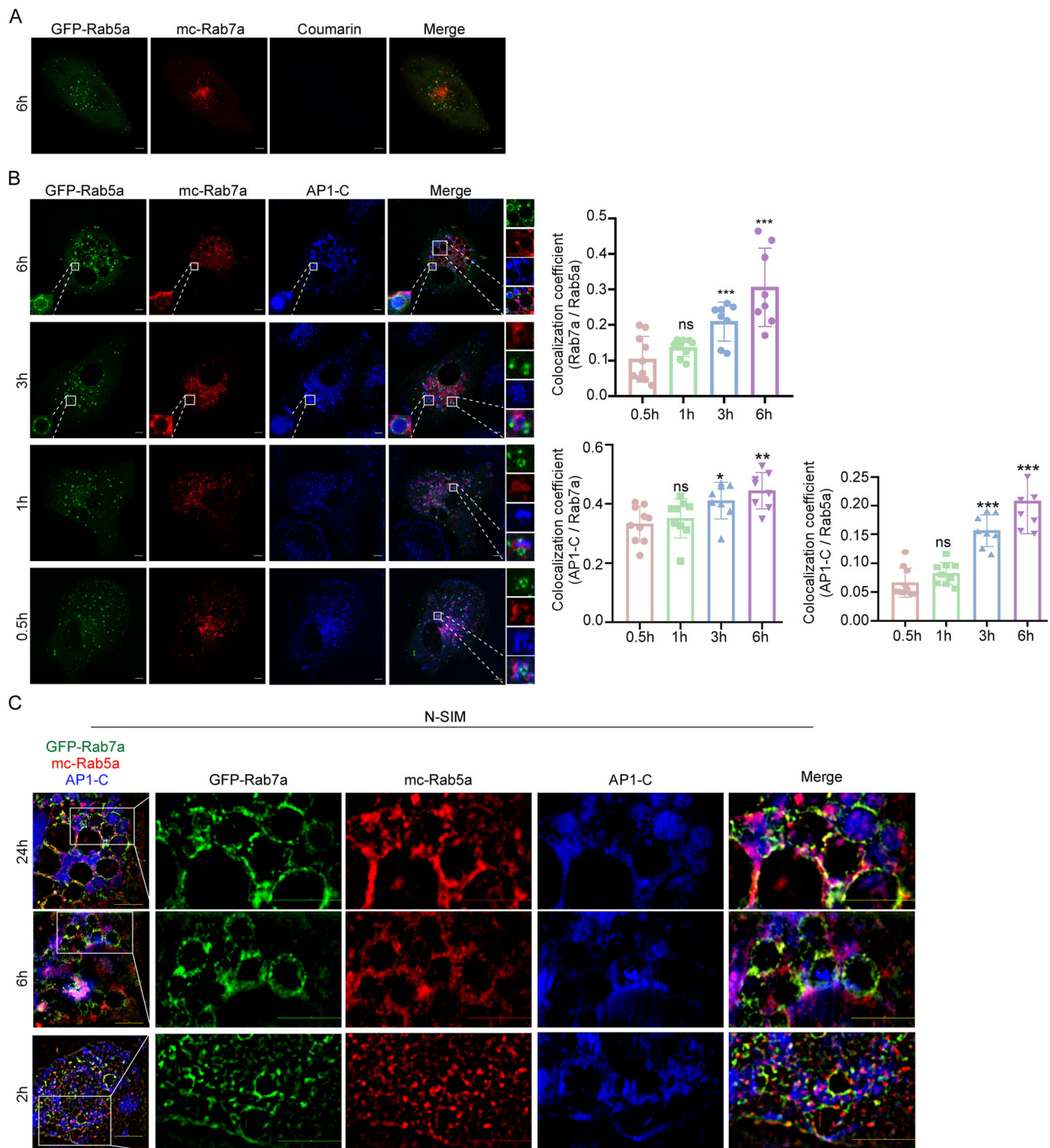
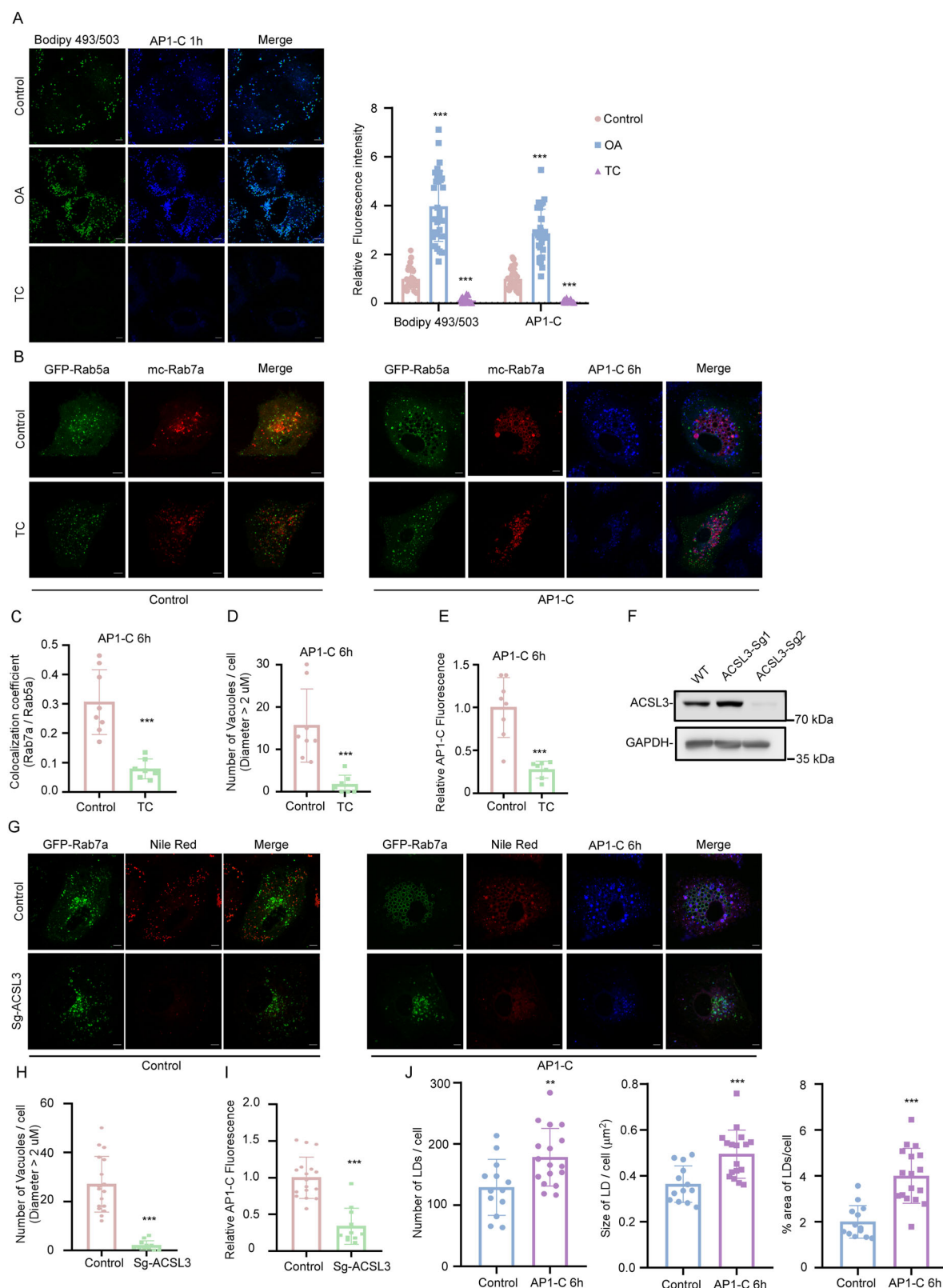


**Fig. 2 | LDs contact with endosomes and are engulfed in intermediate endosomes.** **A, B** A549 cells were transiently transfected with GFP-Rab5a and mc-Rab7a, and then treated with coumarin (10  $\mu$ M) for 6 h (**A**) or AP1-C (10  $\mu$ M) for the indicated time (**B**), followed by confocal imaging. Images were finally captured by the Zeiss 880 microscope with a 63x objective lens. The scale bar is 5  $\mu$ m. Manders colocalization coefficients (MCC) were calculated by ImageJ ( $n = 10, 9, 8$ , and 8 for 0.5 h, 1 h, 3 h, and 6 h, respectively; compared to 0.5 h, for Rab7a/Rab5a,  $p = 0.1697$ ,  $p = 0.0019$ , and  $p = 0.0002$  for 1 h, 3 h, and 6 h, respectively; for AP1-C/Rab7a,  $p = 0.5240$ ,  $p = 0.0151$ , and  $p = 0.0001$  for 1 h, 3 h, and 6 h, respectively; for AP1-C/

Rab5a,  $p = 0.1446$  for 1 h, and  $p < 0.0001$  for 3 h and 6 h). **C** A549 cells were transiently transfected with mc-Rab5a and GFP-Rab7a, then treated with AP1-C (10  $\mu$ M) for the indicated times before being fixed by 4% PFA. Images were captured with the N-SIM with a 100x objective lens ( $n = 3$  for each time point). The scale bar is 1  $\mu$ m. The statistical significance of differences was determined by using the unpaired two-tailed student's  $t$  test. The graphs represented data from three independent experiments, and data quantifications were expressed as mean  $\pm$  s.e.m. \* $p < 0.05$ , \*\* $p < 0.01$ , \*\*\* $p < 0.001$ ; ns: no significance.

(Supplementary Fig. 7D). Likewise, only in cells coexpressing twinstrep-RAB5 and HA-RAB7 treated with AP1, streptavidin beads brought down both RAB5 and RAB7 (Supplementary Fig. 7E). These results suggest that the enlarged endocytic vesicles observed

in cells treated with these triazine analogs are intermediate endosomes. In AP1-C-treated cells, LDs can establish contact with and even become engulfed by these intermediate endosomes (Fig. 2A–C).



### LDs biogenesis is required for the ability of AP1-C to induce enlarged RAB7-RAB5-double positive intermediate endosomes

We previously showed that the triazine compounds activate RAB5 to block early-to-late endosomes transition, thereby inducing enlarged endosomes<sup>23</sup>, and AP1-C, a triazine compound, exclusively label LDs (Fig. 1). Therefore, we reasoned that AP1-C might be routed to endosomes via LDs, thereby inducing enlarged intermediate endosomes. To

assess this, we first treated A549 cells with Oleic acid (OA)<sup>39</sup> or Triacsin C (TC)<sup>40</sup> overnight to promote or inhibit the biogenesis of LDs, respectively, followed by AP1-C treatment. We showed that OA induced the formation of LDs, manifested by the increased fluorescence intensity of Bodipy- and AP1-C-stained cells. In contrast, TC inhibited LDs formation, manifested by the decreased fluorescence intensity of Bodipy- and AP1-C-stained cells (Fig. 3A). These results confirm that AP1-C does label LDs.

**Fig. 3 | Biogenesis of LDs is essential for API-C-induced enlarged intermediate endosomes.** **A** A549 cells were treated with DMSO, Oleic acid (OA) (200  $\mu$ M), or Triacsin C (TC) (5  $\mu$ M) overnight and then co-stained with Bodipy 493/503 (1  $\mu$ M) and API-C (10  $\mu$ M) for 1 h, followed by confocal imaging. The fluorescence intensity of cells was quantified by ImageJ ( $n = 30$  for all columns; compared to the control group, for the Bodipy 493/503 group,  $p < 0.0001$  for both OA and TC; for the API-C group,  $p < 0.0001$  for both OA and TC). **B–E** A549 cells were transiently co-transfected with GFP-Rab5a and mc-Rab7a, treated with DMSO or TC (5  $\mu$ M) overnight, and subsequently treated with DMSO or API-C (10  $\mu$ M) for an additional 6 h before confocal imaging (**B**). The colocalization (MCC) of Rab5a and Rab7a was quantified using ImageJ (**C**) ( $p < 0.0001$ ), the diameter of vacuoles (diameter  $> 2 \mu$ m) was calculated using ZEN Black software (**D**) ( $p = 0.0007$ ), and the fluorescence intensity was quantified using ImageJ (**E**) ( $p < 0.0001$ ). Sample sizes were  $n = 8$  for the control group and  $n = 7$  for the TC-treated group in (**C–E**). **F** Knockdown efficiency of ACSL3 in A549 cells was analyzed by immunoblotting analysis ( $p < 0.0001$ ). **G–J** Control or ACSL3-knockdown cells were transiently

transfected with GFP-Rab7a, and then treated with DMSO or API-C (10  $\mu$ M) for 6 h, followed by treatment with Nile Red (1  $\mu$ M) for 30 min (**G**). Images were finally captured by a Zeiss 880 microscope with a 63x objective lens. The scale bar is 5  $\mu$ m. The number of GFP-Rab7a-positive vacuoles (diameter  $> 2 \mu$ m) in scramble-Sg-expressing cells or ACSL3-Sg-expressing cells was quantified using ZEN black software (**H**) ( $n = 17$  and 11 for Scramble-Sg and Sg-ACSL3, respectively;  $p < 0.0001$ ). The fluorescence intensity of API-C in scramble-Sg-expressing cells or ACSL3-Sg-expressing cells (**I**) ( $n = 17$  and 11 for Scramble-Sg and Sg-ACSL3, respectively;  $p < 0.0001$ ), as well as the number, size, and area of Nile Red-positive LDs in scramble-Sg-expressing cells treated with or without API-C (**J**) were calculated using ImageJ ( $n = 13$  and 17 for control and API-C 6 h, respectively;  $p = 0.0067$  for number of LDs,  $p = 0.0008$  for size of LDs, and  $p < 0.0001$  for % area of LDs). The graphs represented data from three independent experiments. The statistical significance of differences was determined by using the unpaired two-tailed student's  $t$  test, and data quantifications were expressed as mean  $\pm$  s.e.m. \* $p < 0.05$ , \*\* $p < 0.01$ , \*\*\* $p < 0.001$ ; ns: no significance.

Next, we treated the A549 cells coexpressing GFP-RAB5 and mCherry-RAB7 with or without TC overnight, followed by API-C treatment for another 6 h and confocal imaging. We showed that TC pretreatment abolished API-C-induced colocalization between RAB5 and RAB7 (Fig. 3B, C), and enlarged vacuoles (Fig. 3B, D, and Supplementary Fig. 8). Consistently, TC pretreatment markedly inhibited the fluorescence intensity of API-C stained cells (Fig. 3B, E). Whereas OA pretreatment did not affect the ability of API-C to induce large vacuoles (Supplementary Fig. 8). Likewise, ACSL3 knockdown in A549 cells (Fig. 3F) abolished API-C-induced large vacuoles (Fig. 3G, H) and the fluorescence intensity of API-C stained cells (Fig. 3G, I). These results indicate that biogenesis of LDs is required for API-C-induced enlarged intermediate endosomes. Notably, when we quantified the number and size of Nile Red-stained LDs in control cells treated with or without API-C, we found that the size and number of LDs were significantly higher in API-C-treated cells when compared to control cells (Fig. 3J). Since API-C inhibits endosomal trafficking (Supplementary Fig. 3C, D), these results suggest that endosomal trafficking might regulate LD biogenesis or catabolism.

### LDs biogenesis participates in endosomal trafficking

Our results indicate that LDs contact endosomes (Fig. 2), and when LDs biogenesis is inhibited, the ability of triazine compounds to induce large RAB5/RAB7-double positive endosomes is abolished (Fig. 3, and Supplementary Fig. 8). Therefore, LDs biogenesis might participate in endosomal trafficking. We, thus, examined the number of early endosomes (RAB5-positive) and late endosomes (RAB7-positive) in control or ACSL3-knockdown cells. We showed an increase in the number of RAB5-positive early endosomes and a decrease in the number of RAB7-positive late endosomes in cells where ACSL3 was knocked down, as compared to control cells (Fig. 4A, B). Consistently, TC treatment increased the number of RAB5-positive early endosomes and decreased RAB7-positive late endosomes (Fig. 4C, D). In addition, we knocked down GPAT4, an enzyme crucial for triacylglycerol synthesis and LD biogenesis<sup>41,42</sup>. As anticipated, knocking down GPAT4 resulted in a significant reduction of LDs compared to control cells. Similarly to the ACSL3 knockdown, GPAT4-knockdown cells showed an increase in the number of early endosomes and a decrease in the number of late endosomes (Supplementary Fig. 9A, B).

Finally, we assessed whether inhibiting LDs' biogenesis by ACSL3 knockdown affects endosomal trafficking of low-density lipoprotein (LDL). In this assay, when LDL binds to its receptor (LDLR) on the cell surface, the LDL-LDLR complex is internalized via clathrin-mediated endocytosis. The LDL-containing vesicles then fuse with early endosomes. Thereafter, LDL can either be directed to lysosomes for degradation, releasing cholesterol for cellular use, or recycled back to the cell surface along with LDLR<sup>43</sup>. We started this assay by incubating cells with LDL-488 on ice for 1 h. We either fixed these cells

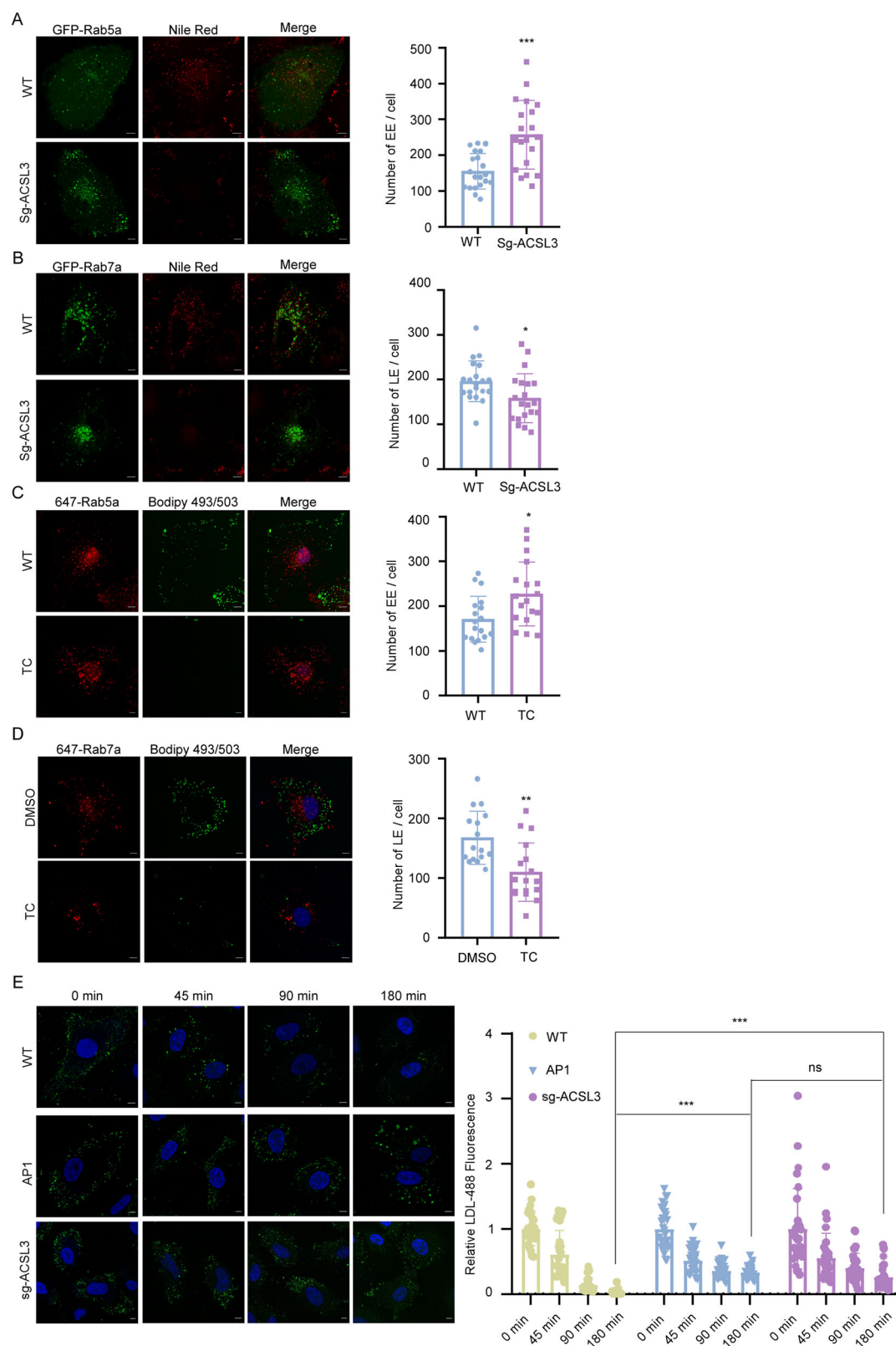
immediately or incubated them at 37 °C for the indicated time to initiate the endocytosis of LDL-488 before fixation. We showed that in control cells, most internalized LDL was degraded around 180 min after being released from cold, whereas in ACSL3-knockdown cells, LDL degradation was significantly delayed. As a control, API, a potent endosomal trafficking inhibitor, also markedly inhibited LDL degradation (Fig. 4E). We also assessed transferrin recycling in cells with defective LD biogenesis. We showed that transferrin trafficking was significantly compromised in ACSL3-knockdown cells and in cells treated with TC (Supplementary Fig. 10). Likewise, GPAT4 knockdown significantly inhibited the degradation of LDLs and the recycling of Transferrin (Supplementary Fig. 9C, D). These results suggest that LDs participate in endosomal trafficking.

### Endosomal trafficking contributes to LDs catabolism

The size and number of LDs were significantly higher in API-C-treated cells when compared to control cells (Fig. 3G, J). Likewise, when cells were treated with Bafilomycin (Baf-A1), a vacuolar ATPase inhibitor which inhibits lysosome fusion with autophagosome or endosome<sup>44–47</sup>, or API, there was a significant augmentation in the fluorescence intensity of Nile red-labeled cells. Conversely, treatment with TC (a LDs inhibitor) notably suppressed the fluorescence intensity of Nile red-labeled cells (Supplementary Fig. 11A). These results suggest that endosomal trafficking might also regulate the catabolism of LDs. Therefore, we examined whether endosomal trafficking is involved in LDs' catabolism. We first knocked down the expression of RAB5 in A549 cells (Fig. 5A). As expected, RAB5 knockdown led to a significant increase in the fluorescence intensity of Bodipy or Nile red-labeled cells as shown by FACS analysis (Supplementary Fig. 11B, C). Confocal imaging analysis further corroborated these findings, showing a significant enhancement in the fluorescence intensity of Bodipy-stained cells upon RAB5 knockdown, when compared to control cells. Moreover, compared to the control cells, the number of LDs in RAB5-knockdown cells was significantly higher, although the size of LDs in RAB5-knockdown cells was relatively smaller (Fig. 5B). Correspondingly, triglyceride levels were substantially elevated in RAB5-knockdown cells when compared to control cells (Fig. 5C). Likewise, expression of a dominant-negative mutant of RAB5, RAB5-S23N<sup>48</sup>, in A549 cells resulted in a marked increase in the fluorescence intensity of Bodipy-stained cells, an increase in the number of LDs, and a decrease in LD size when compared to control cells (Fig. 5D). These results suggest that inhibiting early endosome maturation compromises the catabolism of LDs.

Next, we knocked down the expression of RAB7 in A549 cells (Fig. 6A). We showed RAB7 knockdown, similar to RAB5 knockdown, led to a significant increase in the fluorescence intensity of Bodipy or Nile red-labeled cells as demonstrated by FACS analysis and confocal imaging analysis (Supplementary Fig. 11B, C, and Fig. 6B). RAB7





knockdown also markedly increased the number of LDs (Fig. 6B), and elevated triglyceride levels (Fig. 6C), when compared to control cells. However, RAB7 knockdown failed to affect the size of LDs (Fig. 6B), which is different from RAB5 knockdown (Fig. 5B). Last, we expressed a dominant-mutant of RAB7, RAB7-T22N<sup>49</sup>, or a constitutively-active mutant of RAB7, RAB7-Q67L<sup>49</sup>, in A549 cells, and examined their effects on the size and number of LDs. We showed that the expression

of RAB7-T22N significantly increased both the number of LDs and the fluorescence intensity of Bodipy-stained cells, with little impact on LD size (Fig. 6D), in comparison to control cells, which mirrored the effects of RAB7 knockdown (Fig. 6B). Interestingly, the expression of RAB7-Q67L had the opposite effect, notably reducing both the number and size of LDs, as well as the fluorescence intensity of Bodipy-stained cells, in comparison to control cells (Fig. 6D). In summary, these

**Fig. 4 | Biogenesis of LDs participates in endosomal trafficking.** **A, B** Control or ACSL3-knockdown A549 cells were transiently transfected with GFP-Rab5a (**A**) or GFP-Rab7a (**B**), and then treated with Nile Red (1  $\mu$ M) for 30 min, followed by confocal imaging. The number of Rab5-positive early endosomes (EEs) or Rab7-positive late endosomes (LEs) was quantified by ImageJ ( $n = 20$  for both WT and Sg-ACSL3 in (**A, B**);  $p = 0.0001$  for (**A**), and  $p < 0.0238$  for (**B**)). **C, D** A549 cells were treated with DMSO or TC (5  $\mu$ M) overnight. The cells were then fixed with 4% PFA, immunostained with antibodies against Rab5a (**C**) or Rab7a (**D**), and co-stained with Bodipy 493/503 (1  $\mu$ M) and DAPI (1  $\mu$ g/mL) for 30 min. The number of EEs and LEs was quantified by ImageJ (For **C**,  $n = 18$  for both WT and TC,  $p = 0.0103$ ; for **D**,  $n = 16$  and 17 for WT and TC, respectively, and  $p = 0.0013$ ). **E** Control or ACSL3-

knockdown A549 cells treated with DMSO or API (1  $\mu$ M) were incubated with LDL-488 on ice for 1 h, and then released into the warm medium for the indicated times, and the fluorescence of LDL was calculated by ImageJ ( $n = 30$  for all groups; at 180 min, compared to WT,  $p < 0.0001$  for both API and Sg-ACSL3, while compared to API,  $p = 0.0731$  for ACSL3). Images were captured by a Zeiss 880 microscope with a 63x objective lens. The scale bar is 5  $\mu$ m. The graphs represented data from three independent experiments. The statistical significance of differences was determined by using the unpaired two-tailed student's  $t$  test, and data quantifications were expressed as mean  $\pm$  s.e.m. \* $p < 0.05$ , \*\* $p < 0.01$ , \*\*\* $p < 0.001$ ; ns: no significance.

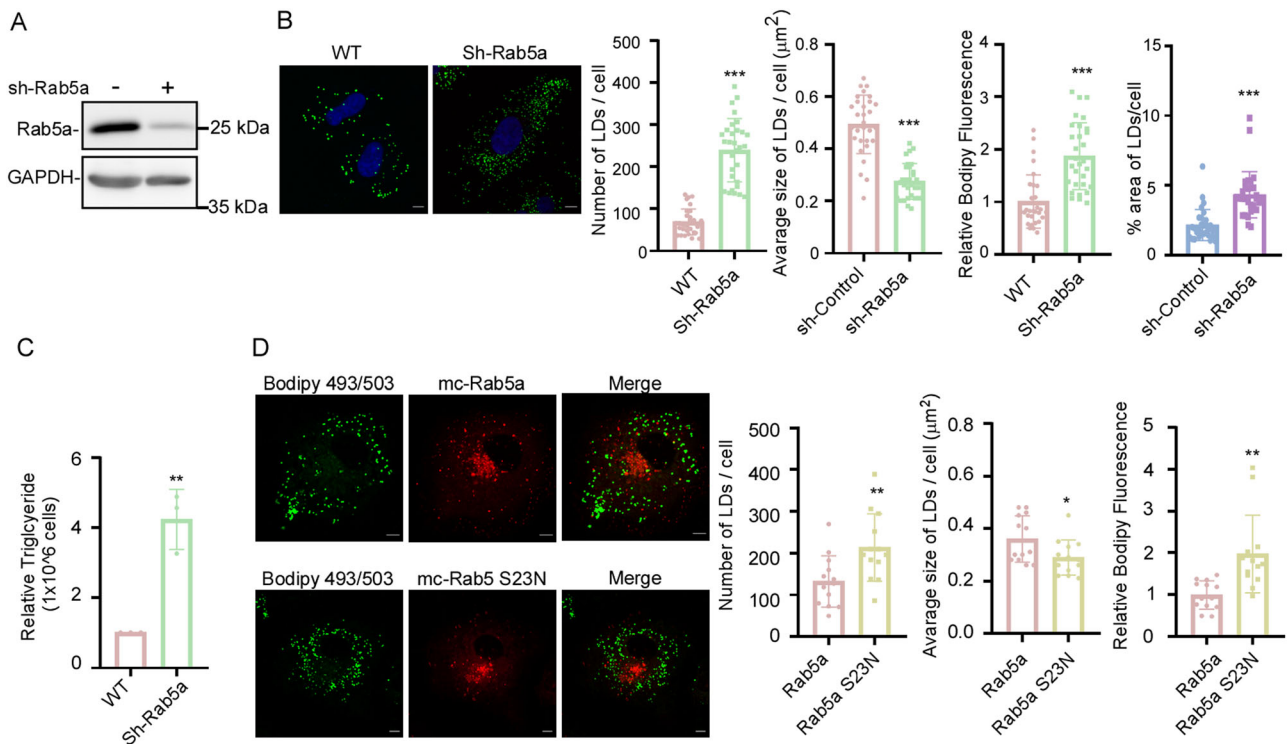


**Fig. 5 | Inhibiting early endosome maturation compromises the catabolism of LDs.** **A** The knockdown efficiency of Rab5a in A549 cells was assessed by western blot analysis ( $n = 3$ ). **B** Control or Rab5a-knockdown A549 cells were fixed by 4% PFA, and stained with Bodipy 493/503 (1  $\mu$ M) and DAPI (1  $\mu$ g/mL) for 30 min. The number, size and area of LDs, as well as the fluorescence intensity of Bodipy 493/503 were quantified by ImageJ ( $n = 30$  for all figures;  $p < 0.0001$  for all figures). **C** The triglyceride level in control or Rab5a-knockdown A549 cells was determined ( $p < 0.0029$ ). **D** A549 cells were transiently transfected with mc-Rab5a or mc-Rab5a-S23N, and then stained with Bodipy 493/503 (1  $\mu$ M) for 30 min. The number and

size of LDs, and fluorescence intensity of Bodipy 493/503 were quantified by ImageJ ( $n = 13$  for all figures;  $p = 0.0080$ ,  $0.0303$  and  $0.0015$  for number of LDs, average size of LDs and relative Bodipy fluorescence, respectively). Images were captured by a Zeiss 880 microscope with a 63x objective lens. The scale bar is 5  $\mu$ m. The graphs represented data from three independent experiments. The statistical significance of differences was determined by using the unpaired two-tailed student's  $t$  test, and data quantifications were expressed as mean  $\pm$  s.e.m. \* $p < 0.05$ , \*\* $p < 0.01$ , \*\*\* $p < 0.001$ ; ns: no significance.

findings suggest that hindering the maturation of late endosomes negatively influences LD catabolism, whereas promoting late endosome maturation enhances LD catabolism.

Given that Rab5, Rab7, and other Rabs have been identified by lipid droplet proteome studies<sup>13–18</sup>, it is possible that Rab5 and/or Rab7 might directly regulate LD biogenesis and catabolism. Therefore, we further knocked down the expression of CCZ1, a subunit of RAB7 GEF that is essential for early-late endosome transition<sup>50,51</sup>, in A549 cells (Fig. 7A). CCZ1 knockdown has been shown to result in the accumulation of large vacuoles<sup>52–54</sup>, like API-C or API treatment (Fig. 2, and Supplementary Fig. 7). Indeed, CCZ1 knockdown resulted in the accumulation of enlarged vacuoles, which are surprisingly RAB5-RAB7-double positive, indicating they are intermediate endosomes (Fig. 7B). This observation is similar to what is seen in API-C or API-treated cells (Fig. 2B, and Supplementary Fig. 7A–C). As expected, CCZ1 knockdown, like API-C treatment (Fig. 3G) or defects in RAB5 or RAB7 (Fig. 5, 6), significantly

inhibited LD degradation, manifested by the increased Nile Red or Bodipy fluorescence intensity and the number and size of LDs in CCZ1-knockdown cells when compared to control cells (Fig. 7C–F). Notably, in CCZ1-knockdown cells, some large LDs were observed within the enlarged intermediate endosomes, as highlighted in the inserts of Fig. 7E. Likewise, CCZ1 knockdown elevated triglyceride levels compared to control cells (Fig. 7G). These results again demonstrate that inhibiting endosomal trafficking compromises LD catabolism.

### The contact between LDs and endosomes is independent of autophagosome biogenesis

Autophagy regulates lipid droplets by breaking them down through a process called lipophagy, where lipid droplets are engulfed by autophagosomes and delivered to lysosomes for degradation<sup>55,56</sup>. Endosomes can fuse with autophagosomes to form amphisomes, which then merge with lysosomes for the degradation of their



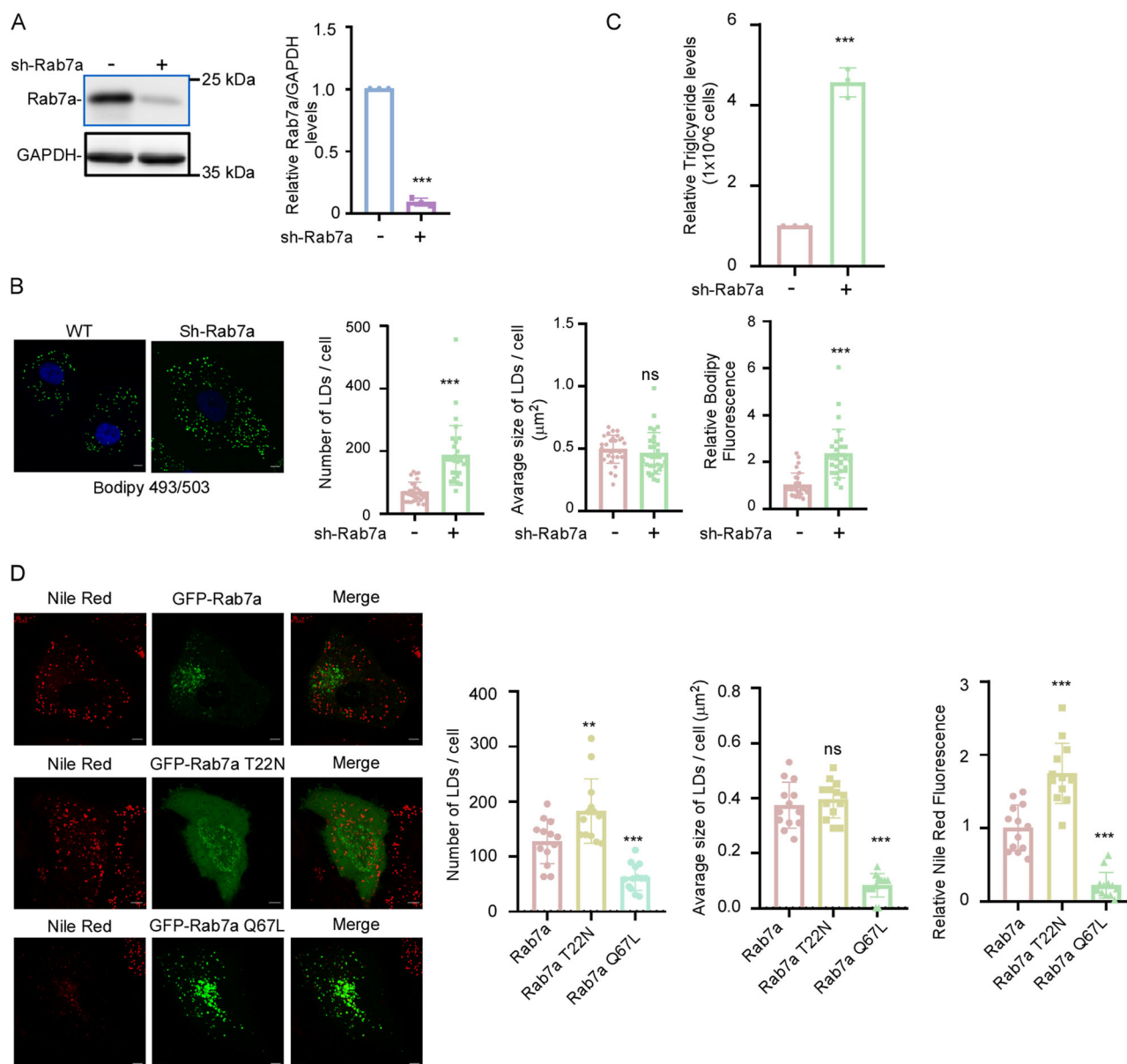


**Fig. 6 | Inhibiting late endosome maturation impedes the catabolism of LDs. A**

The knockdown efficiency of Rab7a in A549 cells was assessed by western blot analysis ( $p < 0.0001$ ). **B** Control or Rab7a-knockdown A549 cells were fixed by 4% PFA, and then stained by Bodipy 493/503 (1 μM) and DAPI (1 μg/mL) for 30 min. The number and size of LDs, and fluorescence intensity of Bodipy 493/503 were quantified by ImageJ ( $n = 30$  for all figures;  $p < 0.0001$  for number of LDs and relative Bodipy fluorescence,  $p = 0.3763$  for average size of LDs). **C** Triglyceride level in control or Rab7a-knockdown A549 cells was determined ( $p < 0.0001$ ). **D** A549 cells were transiently transfected with GFP-Rab7a, GFP-Rab7a-T22N, or GFP-Rab7a-Q67L, and then stained with Nile Red (1 μM) for 30 min. The number and

size of LDs, and fluorescence intensity of Nile Red were quantified by ImageJ ( $n = 13$  for all figures; for number of LDs,  $p = 0.0097$  for Rab7a T22N,  $p < 0.0001$  for Rab7a Q67L; for average size of LDs,  $p = 0.4779$  for Rab7a T22N,  $p < 0.0001$  for Rab7a Q67L; and for relative Bodipy fluorescence,  $p < 0.0001$  for both Rab7a T22N and Rab7a Q67L). Images were captured by a Zeiss 880 microscope with a 63x objective lens. The scale bar is 5 μm. The graphs represented data from three independent experiments. The statistical significance of differences was determined by using the unpaired two-tailed student's *t* test, and data quantifications were expressed as mean  $\pm$  s.e.m. \* $p < 0.05$ , \*\* $p < 0.01$ , \*\*\* $p < 0.001$ ; ns: no significance.

combined cargo<sup>57,58</sup>. Therefore, we assessed whether blocking autophagosome biogenesis affects the interaction of LDs with endosomes. To explore this, we knocked down the expression of ATG7 in A549 cells. ATG7 is a crucial enzyme in autophagy, facilitating the conjugation of ATG12 to ATG5 and the lipidation of LC3, which are essential steps for autophagosome formation and expansion<sup>59</sup>. When compared to control cells, ATG7 knockdown not only resulted in the decreased levels of LC3-II and increased level of p62, but also abolished the ability of Baf A1-induced LC3-II and p62 in A549 cells, indicating that ATG7 knockdown abolishes autophagic flux (Supplementary Fig. 12A). Confocal imaging analysis showed that ATG7 knockdown had little effect

on the colocalization between Bodipy positive puncta and RAB5 or RAB7 positive endosomes (Supplementary Fig. 12B, C). Likewise, ATG7 knockdown had little effect on the colocalization between AP1-C positive puncta and RAB5 or RAB7 positive endosomes (Supplementary Fig. 12D). These results indicate that blocking autophagosome biogenesis does not affect the interaction of LDs with endosomes.

## Discussion

One significant finding of this current study is the characterization of the previously unknown reciprocal interplay between LDs and endosomes. We screened and synthesized a fluorophore-conjugated

triazine compound, API-C, and showed that this probe specifically labels LDs of all stages in live cells. API-C is also an endosomal trafficking inhibitor that prevents the early to late endosome transition, resulting in the accumulation of enlarged intermediate endosomes,

which are RAB5 and RAB7 double positive. By applying API-C to stain live cells, we observed that LDs not only contact endosomes, but also are engulfed into these endosomes. Moreover, there is a reciprocal regulation between LDs and endosomes. On the one hand, the

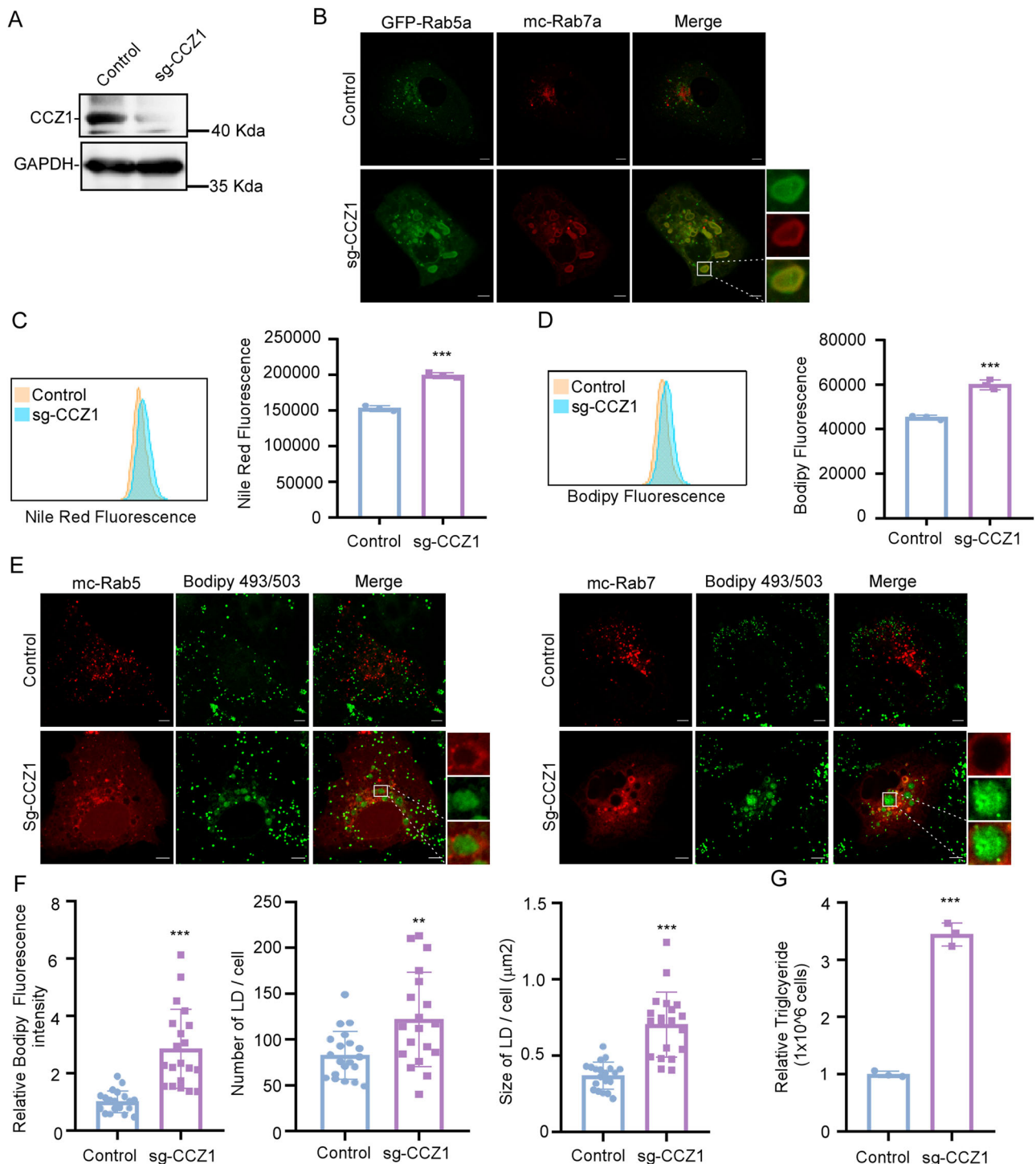


**Fig. 7 | CCZ1 knockdown compromises LD biogenesis.** **A** Knockdown efficiency of CCZ1 in A549 cells was assessed by immunoblot analysis ( $n = 3$ ). **B** Control or CCZ1-knockdown A549 cells were transiently transfected with GFP-Rab5 and mc-Rab7 ( $n = 12$ ), followed by confocal imaging. **C**, **D** Control or CCZ1-knockdown A549 cells were stained with Nile Red (1  $\mu$ M) (**C**) or Bodipy 493/503 (1  $\mu$ M) (**D**) for 1 h, followed by flow cytometry (**C**:  $p = 0.0002$ ; **D**:  $p = 0.0006$ ). **E**, **F** Control or CCZ1-knockdown A549 cells were transiently transfected with mc-Rab5a or mc-Rab7a, and then stained with Bodipy 493/503 (1  $\mu$ M) for 1 h before fixing by 4% PFA, followed by confocal imaging (**E**). The number and size of LDs, and fluorescence intensity of

Bodipy 493/503 were quantified by ImageJ (**F**) ( $n = 20$  for all figures; for the number of LDs,  $p = 0.0046$ ; for relative Bodipy fluorescence and LD size,  $p < 0.0001$ ). Images were captured by a Zeiss 880 microscope with a 63x objective lens. The scale bar is 5  $\mu$ m. **G** Triglyceride level in control or CCZ1-knockdown A549 cells was determined ( $p < 0.0001$ ). The graphs represented data from three independent experiments. The statistical significance of differences was determined by using the unpaired two-tailed student's  $t$  test, and data quantifications were expressed as mean  $\pm$  s.e.m. \* $p < 0.05$ , \*\* $p < 0.01$ , \*\*\* $p < 0.001$ ; ns: no significance.

biogenesis of LDs promotes endosomal trafficking, while on the other hand, endosomal trafficking is involved in the catabolism of LDs.

It is known that the catabolism of LDs is mediated by lipolysis and/or fusion with lysosomes or autophagosomes for degradation<sup>55,60–65</sup>. Here, we showed that some LDs are degraded via endosomes, likely a route to lysosomes. Therefore, inhibiting endosome maturation by RAB5, RAB7, or CCZ1 knockdown, or expression of their dominant-negative mutants, or application of endocytosis inhibitors, such as Baf-A1 and AP1, resulted in the accumulation of LDs, and increased levels of triglyceride (Figs. 5–7, and Supplementary Fig. 11). On the other hand, expression of a constitutively active mutant RAB7, which facilitates endosomal trafficking, promotes LDs catabolism (Fig. 6D). Therefore, our results indicate that endosomal trafficking is another cellular process involved in LDs catabolic process. Future efforts are needed to identify the protein complex responsible for the contacts and fusion between LDs and endosomes.

LDs biogenesis involves the homotypic fusion of endocytic vesicles<sup>66</sup>. We showed that inhibiting LD biogenesis, either by TC (an LD inhibitor) treatment or knockdown of ACSL3 or GPAT4, compromises endosomal trafficking. This is evidenced by an increase in early endosome numbers and a decrease in late endosome numbers under these conditions compared to control cells (Fig. 4, and Supplementary Fig. 9). These observations suggest that LDs play a critical role in endosomal maturation, likely through their contact sites with endosomes. Such contacts may enable LDs as hubs to deliver specific effectors, such as specific lipid species (e.g., phospholipids or neutral lipids) or signaling proteins originating from the ER, which are essential for the maturation process. For example, LDs-associated proteins could serve as scaffolds or interaction hubs for proteins (e.g., RAB5 effectors or regulators) involved in endosomal trafficking. Identifying these key effectors or lipid species routed from LDs to endosomes, potentially using advanced lipidomics and proteomics approaches, will be an important avenue for future research and could provide critical insights into the molecular interconnections between these organelles.

Our findings further indicate that LDs are involved in mediating the effects of triazine compounds on endocytic vesicles. Specifically, we showed that TC treatment or ACSL3 knockdown abolishes the ability of triazine compounds to induce homotypic fusion of endocytic vesicles (Fig. 3 and Supplementary Fig. 8). Since these triazine compounds initially localize to LDs (Fig. 1 and Supplementary Fig. 4), LDs may serve as platforms for either carrying the compounds' effectors or enabling the compounds to interact with their effectors. For example, the effector CapZ might be recruited to endosomes upon LD-endosome contact. This recruitment likely facilitates the activation of RAB5 and the subsequent recruitment of RAB7 to intermediate endosomes, thereby modulating the transition from early to late endosomes.

We have previously shown that triazine compounds, like V1 or 6J1, potentially inhibit endosomal trafficking by promoting homotypic fusion of endosomes<sup>23–26,67,68</sup>. It is widely accepted that the recruitment of RAB7 to endosomes is preceded by the inactivation and release of RAB5 from early endosomes<sup>52,69</sup>. RAB5 activity is much higher in cells treated with triazine compounds when compared to control cells<sup>24,25</sup>. Thus, we initially thought that these enlarged endocytic vesicles induced by these triazine compounds are matured early endosomes<sup>24</sup>. In the current study, we further showed that these enlarged endocytic vesicles induced by triazine compounds are intermediate endosomes, which are both RAB5 and RAB7 positive (Figs. 2, 3, and Supplementary Fig. 7). These results suggest that these triazine compounds stop endosomal trafficking by preventing the transition of early endosomes to late endosomes. Similarly, the enlarged vacuoles in CCZ1-deficient cells were generally assumed to be early endosomes<sup>52–54</sup>, since it is widely accepted that the CCZ1-Mon1 complex not only functions as a

Rab7 GEF but also aids in recruiting Rab7 to late endosomes, thereby facilitating the transition from early to late endosomes. Thus, it is surprising to find Rab7 also present in the enlarged Rab5-positive endosomes in CCZ1-knockdown cells (Fig. 7B), suggesting they are intermediate endosomes rather than purely early or late endosomes<sup>52</sup>. These results also suggest that the recruitment of RAB7 to endocytic vesicles is independent of RAB5 inactivation or at least that RAB5 inactivation or release from early endosomes is not a prerequisite for RAB7 recruitment to intermediate endosomes. It remains to assess whether RAB7 in these intermediate endosomes induced by triazine compounds is active.

There is weak colocalization between RAB7-positive puncta and LDs labeled with BODIPY or Nile Red in A549 cells due to the highly dynamic nature of endocytic vesicles and LDs (Supplementary Fig. 1). When endosomal trafficking was arrested at intermediate endosome stage by either AP1-C treatment (Fig. 2 and Supplementary Fig. 6) or CCZ1 knockdown (Fig. 7), clear contacts between LDs and endosomes were observed. Interestingly, notable colocalization of RAB7-positive puncta with Oil Red O (ORO)-stained LDs was observed in hepatocytes. Starvation further enhanced this colocalization to promote lipolysis, although these observations were not accompanied by quantification or statistical analysis<sup>6</sup>. The discrepancy between these results can be attributed to the functional states of LDs, differences in dyes used to label LDs, cell types, experimental conditions, and imaging techniques. For example, starvation, which greatly increases the size and number of LDs<sup>2,70</sup>, might enhance their interaction with RAB7-positive puncta. Also, ORO is specific for neutral lipids and stains mature lipid droplets in fixed cells but can also mark other lipid-rich structures or pathological lipid deposits<sup>71,72</sup>. BODIPY and Nile Red, on the other hand, are dyes that can stain LDs in both live and fixed cells<sup>20,72,73</sup>.

AP1-C treatment or CCZ1 knockdown arrested endosomal trafficking at intermediate endosomes. Consequently, in AP1-C treated cells or CCZ1-knockdown cells, we observed the clear contact between LDs and intermediate endosomes (Figs. 2 and 7). Yet, it is possible that LDs also interact with early or late endosomes under different conditions. Characterizing the maturation process of LDs as they interact with early endosomes and transition to late endosomes could enhance our understanding of lipid metabolism and cellular homeostasis. However, the highly dynamic nature of both endosomal trafficking and LD maturation presents significant technical challenges. To thoroughly investigate these processes, it would be essential to develop specific probes that can label LDs and endosomes at different stages and to create techniques to arrest these structures at precise points in their lifecycle.

Nevertheless, our study underscores the reciprocal interaction between LDs and endosomes, two highly dynamic organelles. Furthermore, our findings highlight that endosomal trafficking is another essential cellular process responsible for LDs catabolism, contributing to maintaining lipid homeostasis.

## Methods

### General equipment, chemicals, and reagents in chemical synthesis

All chemicals were purchased from commercial sources unless otherwise specified. HRMS were obtained with a MAT95XP (Thermo) mass spectrometer or HPLC-High Resolution Mass Spectrometer (Sciex X500R Q-TOF). The purity of the compound for bioactivity study was confirmed > 95% by high-performance liquid chromatography (HPLC) analysis using a Shimadzu Prominence System equipped with a C18 column (Phenomenex, Gemini, 5  $\mu$ m, 110 Å, 250 X 4.6 mm).

### Chemical synthesis of AP1-coumarin

The chemical synthesis of AP1-coumarin shown in Fig. S3A includes the following steps<sup>26,74</sup>:



**(1) Synthetic method of S2.** 2-pyridin-2-ylethanamine (2 equiv.) and Et<sub>3</sub>N (1.5 equiv.) were dissolved in anhydrous DCM, and cooled to 4 °C on an ice bath. 9-Bromo-1-nonanol (1 equiv.) in anhydrous DCM was added dropwise into the mixture. It was stirred overnight (16–18 h) at room temperature. The solvent was then removed under vacuum, and water was added. The product was extracted by EA, and purified by column chromatography as a colorless oil (yield ~80%).

**(2) Synthetic method of 1a.** Morpholine (1 equiv.) in acetone solution was added dropwise in cyanuric chloride (1.1 equiv.) and K<sub>2</sub>CO<sub>3</sub> (1.5 equiv.) in acetone solution on an ice bath; the mixture was then stirred overnight (16–18 h) at room temperature. The solvent was then evaporated under vacuum, and the solid was dissolved in ethyl acetate (EA), washed three times with water, and dried with Na<sub>2</sub>SO<sub>4</sub>. The crude product was further purified by column chromatography to obtain 1a as a white solid (yield ~78%).

**(3) Synthetic method of 2a-OH.** S2 in acetone solution (1 equiv.) was added dropwise in 1a (1.1 equiv.) and K<sub>2</sub>CO<sub>3</sub> (1.5 equiv.) in acetone solution on an ice bath. The mixture was stirred overnight (16–18 h) at room temperature. The solvent was then evaporated under vacuum, and the residues were dissolved in EA, washed three times with water, and dried with Na<sub>2</sub>SO<sub>4</sub>. The crude product was further purified by column chromatography to obtain 2a-OH as white oil (yield ~72%).

**(4) Synthetic method of API-OH.** (i) NH<sub>2</sub>NH<sub>2</sub> (10 equiv.) in THF solution was added dropwise into 2a-OH (1 equiv.) THF solution, and the mixture was stirred and refluxed for 1–2 h. The solvent was evaporated under a vacuum, and the solid was dissolved in EA, washed three times with water, and dried with Na<sub>2</sub>SO<sub>4</sub>. The crude product 3a-OH was concentrated and used for the next step without further purification; (ii) 3-Iodobenzaldehyde (1.1 equiv.) in ethanol solution was added dropwise into 3a-OH (1 equiv.) ethanol solution with stirring, then 5–6 drops of acetic acid were added. The mixture was allowed to stir at room temperature for 1–2 h. The solvent was then evaporated under vacuum, and the crude product was further purified by column chromatography to obtain a white solid (yield ~65%).

**(5) Synthetic method of API-Coumarin.** Coumarin (1 equiv.), N,N,N',N'-tetramethylchloroformamidinium hexafluorophosphate (TCFH, 1.1 equiv.), and N-methylimidazole (NMI, 3.5 equiv.) were combined in a 25 mL flask. Afterward, 2 mL of MeCN and 1 mL of DMF were added to the flask, and the resulting solution was stirred for 5 min at room temperature. Then, API-OH (1.0 equiv.) was added to the mixture and stirred at room temperature for 24 h. Finally, the solvent was evaporated under reduced pressure and the crude product was purified over preparative HPLC and lyophilized to obtain the API-Coumarin.

### Cell culture

A549, HepG2, HeLa or HEK293T cells were cultured in DMEM (Gibco, 12800082) supplemented with 10% fetal bovine serum (FBS; Gibco, 10500064) plus 1% penicillin/streptomycin (P/S; Gibco, 15140122). The cells were maintained at 37 °C with 5% CO<sub>2</sub> and 95% humidity. Cells were passaged every two to three days.

### Antibodies and reagents for cell experiments

Bafilomycin A1 (MCE, #HY-100558), LDL-488 (Invitrogen, #L23380), Transferrin-488 (Invitrogen, #T13342), Lipid TOX Deep Red (Invitrogen, #H34477), Cell lysis buffer (Beyotime, #P0013), ProLong™ Diamond Antifade (Thermo Fisher, #P36970), Nile Red (Invitrogen, #N1142), BODIPY™ 493/503 (Invitrogen, D3922), Tricasin C (Aladdin, #76896-80-5), Oleic acid (MCE, #HY-N1446), Strep-Tactin (IBA, #2-1201-010), anti-Rab5 (Cell signaling, #46449), anti-Rab7 (Abcam, ab137029), anti-ADRP (protientech, #15294-1-AP), anti-ATG7 (Protientech, #10088-2-AP), anti-GPAT4 (Protientech, #16762-1-AP), anti-CCZ1 (Protientech, #22159-1-

AP), anti-p62 (cell signaling technology, #5114S), anti-TGN 46 (Biorad, #AHP500GT), anti-HSP70 (Santa Cruz, #sc-32239), anti-LC3 (Novus, NB100-2220), anti-GM130 (Protientech, 11308-1-AP), anti-α-Tubulin (Protientech, #11224-1-AP), anti-HA tag (Sigma, #11867423001), Anti-Myc tag (Proteintech, 67447-1-Ig), anti-ACSL3 (Protientech, 20710-1-AP), anti-Actin (Proteintech, 66009-1-Ig), anti-GAPDH (Proteintech, 60004-1-Ig).

### Plasmids

pEGFP-C1-ADRP (addgene, #87161), mcherry-ACSL3 (addgene, #87158), GFP-Rab5 (addgene, #174454), mcherry-Rab5 (addgene, #55126), mcherry-Rab5 S23N, GFP-Rab7 (addgene, #61803), mcherry-Rab7 (addgene, #55127), GFP-Rab7 T22N (addgene, #28048), GFP-Rab7 Q67L (addgene, #28049), pCDNA3.1-Twinstrep Rab5 (Elife. 2021 Nov 19;10:e65910), pCDNA3.1-Twinstrep-Rab7 (GUANGZHOU IGE BIOTECHNOLOGY LTD), myc-Rab5 (Elife. 2021 Nov 19;10:e65910), HA-Rab7 (GUANGZHOU IGE BIOTECHNOLOGY LTD), mcherry-HSD17B11 (MIAOLING BIOLOGY), GFP-LiveDrop (MIAOLING BIOLOGY).

### Gene knockdown (KD) in A549 cells

shRNA and sg-RNA sequences were designed by GUANGZHOU IGE BIOTECHNOLOGY LTD or MIAOLING BIOLOGY. shRNA was cloned into the pLKO.1 lentiviral vector and sgRNA was cloned into the lentiCRISPR-V2-puro vector. ACSL3-SgRNA-1: GCTTTCTCACGGATGCGCAT; ACSL3-SgRNA-2: GTTGATGGAAAGCCACCGACC; Sh-Rab5a: CAAGGCCGACCTAGCAAATAA; Sh-Rab7a: GGAAGAAAGTGTGCTG AAGG; CCZ1-SgRNA: GATTAGAGAAATCTTCCAT; GPAT4-SgRNA: GCTACCTTGAGAATGGAGCG. ATG7 Sg-RNA: GCCAGCTCGCTTAA-CAT. Lentivirus was packaged by using HEK293T cells. The stable cell line was constructed after infecting with lentivirus and selecting by appropriate antibiotics. The knockdown efficiency was analyzed by immunoblotting.

### Immunoblotting analysis

Cells were lysed in cell lysis buffer with protease inhibitors, and protein concentration was measured by the Bradford Protein Assay. Proteins were loaded on SDS-PAGE gels, subjected to electrophoresis, and then transferred onto PVDF membranes (Millipore, ISEQ00010). Then, the membranes were blocked with 5% BSA in TBST (TBS containing 0.1% Tween-20) for 1 h at room temperature. After incubating with indicated primary antibodies at 4 °C overnight, the membranes were washed with TBST (3 × 5 min). After incubating with appropriate HRP-conjugated secondary antibodies for 1 h at room temperature, images were finally captured by ChemiDoc. with using chemiluminescence substrate.

### Co-munoprecipitation

HEK293T cells were transfected with appropriate plasmids, treated with/without compound for the indicated time, and then lysed in CA630 buffer before being incubated with Strep-Tactin Sepharose (IBA, 2-1201-010) at 4 °C overnight. The beads were then washed for five times with CA630 buffer, and finally subjected to immunoblotting analysis.

### Immunofluorescence staining

Cells were fixed by 4% PFA for 15 min and then permeabilized with PBS containing 0.1% triton X-100 for 15 min at room temperature. After blocking with 5% BSA for 30 min at room temperature, cells were incubated with the indicated primary antibodies at 4 °C overnight. Then, cells were incubated with indicated Alexa Fluor® -conjugated secondary antibody for 1 h at room temperature, stained with indicated dyes for 30 min, and then washed with PBS for 3–4 times. Cells were finally mounted under a glass coverslip with ProLong Diamond Antifade. Images were captured by Carl Zeiss LSM 880 with a 63x oil objective and analyzed with the ZEISS ZEN black or ImageJ software. All the confocal images were taken and analyzed in a single plane. For

image collection, Ex. / Em.: DAPI: 408 nm/410–490 nm; Alexa Fluor 488: 488 nm/495 nm–540 nm; Alexa Fluor 647: 633 nm/ 640 nm–750 nm; Bodipy: 493/503 488 nm/495 nm–540 nm; Nile Red: 561 nm/570 nm–630 nm; Lipid Tox: 633 nm/ 640 nm–750 nm.

### Confocal image of live cells

Cells were seeded overnight at 70–80% confluency on confocal dishes (Mattek, P35G-1.5-14-C). Cells were then transfected with or without fluorescent constructs. The following day, cells were stained with or without the compound. Images were directly captured by a Carl Zeiss LSM 880 confocal microscope by using 63× oil objective and analyzed with the ZEISS ZEN black or ImageJ software. All the confocal images were taken and analyzed in a single plane.

### SIM image

A549 cells were co-transfected with GFP-Rab7a and mCherry-Rab5a, and stained with API-C for different time points. Cells were then fixed by 4% PFA. Images were captured by the Nikon N-SIM system in 3D structured illumination mode on an Eclipse Ti-E microscope equipped with a 100×/1.49 NA oil immersion objective, 405 nm diode laser, 488 and 561 nm solid-state lasers (coherent), and an EM-CCD camera (DU-897, Andor Technology). 15 raw images were captured at different orientations of the structured illumination to generate the super-resolved image, and the final SIM image was reconstructed by using NIS-Elements software. For image collection, Ex. / Em.: API-C: 408 nm/410–490 nm; Bodipy: 493/503 488 nm/495 nm–540 nm; Nile Red: 561 nm/570 nm–630 nm; mCherry: 561 nm/570–630 nm; GFP: 488 nm/495–540 nm.

### Image analysis

All analyses were carried out on single-plane images using Zen Black software or ImageJ. For colocalization analysis, Manders' colocalization coefficient (MCC) or Pearson's correlation coefficient (PCC) was used. Briefly, PCC was employed to quantify the two signals that mostly co-occur on the same cellular structures (e.g., LDs) and whose fluorescent signals fit a single linear relationship, satisfying the requirements of PCC. MCC was used to quantify the two signals requiring a threshold to distinguish an object from the background (e.g., Rab7) or when there is only partial overlap, indicating co-distribution in the same cellular structures. For counting the number or size of LDs and endosomes, the "Analyze Particles" plugin in ImageJ was used. The "Watershed" function was employed to separate connected components, and the "Fill Holes" technique was used to fill the "particles" (e.g., Rab7) with background subtracted. Fluorescence intensity and area of lipid droplets were measured using ImageJ.

### LDL trafficking assay

Cells grown on a coverslip in 24-well plate were starved overnight and treated with or without API. Cells were then washed with ice-cold PBS for three times and incubated on ice in an uptake medium (20 mM HEPES (pH 7.5), DMEM, and 2% BSA) containing 2.5 µg/ml Alexa Fluor 488–LDL for 1 h. After the incubation, unbound ligands on the cells were washed out by ice-cold PBS three times. Cells from one of the wells were fixed to indicate the total LDL bound to cells. Other cells were transferred to the 37 °C incubator and fixed at the indicated time point. Images were captured with a Carl Zeiss LSM 880 confocal microscope using 63×oil objective.

### Transferrin recycling assay

Cells grown on a coverslip in 24-well plate were cultured overnight in completed medium and treated with or without TC. Cells were then washed with ice-cold PBS for three times and incubated on ice in an uptake medium (20 mM HEPES (pH 7.5), DMEM, and 2% BSA) containing 25 µg/ml Alexa Fluor 488–Transferrin for 1 h. After the incubation, unbound ligands on the cells were washed out by ice-cold PBS

three times. Cells from one of the wells were fixed to indicate the total transferrin bound to cells. Other cells were transferred to the 37 °C incubator and fixed at the indicated time point. Images were captured with a Carl Zeiss LSM 880 confocal microscope using 63×oil objective.

### DQ-BSA trafficking assay

Cells were seeded in 6-well plates. On the following day, cells were pretreated with DMSO, API, API-C or Baf A for 4 h, and then incubated with DQ-BSA green for 4 h in the trafficking buffer (DMEM + 1% serum + 1% NEAA + 1% GlutaMax). Cells were then trypsinized, collected, and washed with PBS. After resuspension in 500 µL PBS, cells were immediately analyzed by flow cytometry via FITC channel. Fluorescence intensity was analyzed using FlowJo software.

### FACS analysis

Cells were seeded in 6-well plate. On the following day, cells were pretreated with or without indicated compounds for 6 h, and then stained with Nile Red or Bodipy 493/503 for 30 min. Cells were then trypsinized, collected, and washed with PBS. After resuspended in 300 µL PBS, cells were immediately analyzed by flow cytometry. Nile Red was detected via PE channel while Bodipy 493/503 was detected via FITC channel. Fluorescence intensity was calculated using FlowJo software.

### Lipid droplets isolation

Cells were treated with 200 µM Oleic acid (OA) overnight and then co-treated with compounds for 6 h. Cells were then collected after washing 3 times with PBS. The LDs were finally isolated by the LD Isolation Kit (CELL BIOLABS, #MET-5011) according to manufacturer's protocol.

### Triglyceride measurement

Triglyceride level was measured by using the triglyceride level test kit (Applygen, E1013). Briefly, cells were plated in 6-well plate. On the following day, cells were then collected, washed by PBS, and lysed by lysis buffer at room temperature for 10 min. The supernatant was transferred and heated at 70 °C for 10 min. It was then centrifuged at 2000 rpm for 5 min, and the supernatant was collected for triglyceride testing according to the manufacturer's protocol.

### Stability of API-C

For stability in different buffers, API-C was incubated in the buffer with pH values of 4.5, 5.0, 5.5, or 6.0 for the indicated time, and subjected to LC-MS analysis. For stability in cells, A549 cells were treated with API-C for 6 h or 24 h, cells were then lysed. The lysate was then concentrated and submitted for LC-MS analysis. The excitation wavelength at 420 nm was used for the detection of API-C and coumarin. To assess the stability of API-C in cells after treatment with thapsigargin (TG) or NH<sub>4</sub>Cl, A549 cells were pre-treated with API-C for 1 h, followed by co-treatment with 1 µM TG or 10 mM NH<sub>4</sub>Cl for 6 h or overnight. The cells were then analyzed using a microreader with excitation at 410 nm and emission at 460 nm. Alternatively, the cells were lysed, and the lysate was concentrated and submitted for LC-MS analysis. The excitation wavelength at 420 nm was used for the detection of API-C and coumarin.

### Cell counting kit-8 assay

Cells were plated on 96 well plate overnight. After treatment, the medium was aspirated carefully, and 100 µL fresh medium containing 10 µL Cell Counting Kit-8 (CCK8) solution (Beyotime, #C0038) were added into each well. Cells were incubated at 37 °C for 4 h. After incubation, the plate was scanned immediately by the microreader with the OD absorbance at 450 nm. Cell viability was calculated with OD at 450 nm by GraphPad.

### Correlative light and electron microscopy (CLEM)

Cells were seeded overnight on confocal dishes (MatTek, P35G-1.5-14-C) to reach 70–80% confluency. They were then treated with API-C (10  $\mu$ M) for 4 h, followed by staining with Bodipy (1  $\mu$ M) for 1 h. The cells were fixed with 4% paraformaldehyde (PFA) containing 1% glutaraldehyde to preserve cellular structures. Regions of interest were identified during confocal imaging using a Zeiss 980 microscope with a 63 $\times$  lens, employing tile scanning and z-stacking to acquire high-resolution images. These images served as a reference for locating specific areas for further electron microscopy analysis.

Following fixation, the samples were embedded in resin, and ultrathin sections of the marked regions were prepared using an ultramicrotome and mounted onto copper grids. Transmission electron microscopy (TEM) was performed to obtain high-resolution images of the regions of interest. Finally, confocal and TEM images were aligned and correlated using Photoshop to integrate the light and electron microscopy data for detailed structural analysis.

### Statistical analysis

Data are presented as the mean  $\pm$  the standard error of the mean. The statistical significance of differences was determined by using the unpaired two-tailed student's *t* test.  $P < 0.05$  was used to determine whether a result was significant. \*,  $P < 0.05$ ; \*\*,  $P < 0.01$ ; and \*\*\*,  $P < 0.001$ .  $P > 0.05$  was considered not significant (NS).

### Reporting summary

Further information on research design is available in the Nature Portfolio Reporting Summary linked to this article.

### Data availability

All data supporting the findings of this study are available within the Article, Supplementary Information, and Source Data files. Source data are provided with this paper.

### References

- Herker, E., Vieyres, G., Beller, M., Krahmer, N. & Bohnert, M. Lipid droplet contact sites in health and disease. *Trends Cell Biol.* **31**, 345–358 (2021).
- Olzmann, J. A. & Carvalho, P. Dynamics and functions of lipid droplets. *Nat. Rev. Mol. Cell Biol.* **20**, 137–155 (2019).
- Onal, G., Kutlu, O., Gozuacik, D. & Dokmeci Emre, S. Lipid droplets in health and disease. *Lipids Health Dis.* **16**, 128 (2017).
- Drizyte-Miller, K., Schott, M. B. & McNiven, M. A. Lipid droplet contacts with autophagosomes, lysosomes, and other degradative vesicles. *Contact (Thousand Oaks)* **3**, 1–13 (2020).
- Renne, M. F. & Hariri, H. Lipid droplet-organelle contact sites as hubs for fatty acid metabolism, trafficking, and metabolic channeling. *Front Cell Dev. Biol.* **9**, 726261 (2021).
- Schroeder, B. et al. The small GTPase Rab7 as a central regulator of hepatocellular lipophagy. *Hepatology* **61**, 1896–1907 (2015).
- Menon, D. et al. ARL8B mediates lipid droplet contact and delivery to lysosomes for lipid remobilization. *Cell Rep.* **42**, 113203 (2023).
- Huotari, J. & Helenius, A. Endosome maturation. *EMBO J.* **30**, 3481–3500 (2011).
- Cullen, P. J. & Steinberg, F. To degrade or not to degrade: mechanisms and significance of endocytic recycling. *Nat. Rev. Mol. Cell Biol.* **19**, 679–696 (2018).
- Murphy, J. E., Padilla, B. E., Hasdemir, B., Cottrell, G. S. & Bunnett, N. W. Endosomes: a legitimate platform for the signaling train. *Proc. Natl Acad. Sci. USA* **106**, 17615–17622 (2009).
- Maxfield, F. R. Role of endosomes and lysosomes in human disease. *Cold Spring Harb. Perspect. Biol.* **6**, a016931 (2014).
- Schulze, R. J. et al. Direct lysosome-based autophagy of lipid droplets in hepatocytes. *Proc. Natl. Acad. Sci. USA* **117**, 32443–32452 (2020).
- Krahmer, N. et al. Protein correlation profiles identify lipid droplet proteins with high confidence. *Mol. Cell Proteom.* **12**, 1115–1126 (2013).
- Larsson, S., Resjo, S., Gomez, M. F., James, P. & Holm, C. Characterization of the lipid droplet proteome of a clonal insulin-producing beta-cell line (INS-1 832/13). *J. Proteome Res.* **11**, 1264–1273 (2012).
- Rasineni, K., McVicker, B. L., Tuma, D. J., McNiven, M. A. & Casey, C. A. Rab GTPases associate with isolated lipid droplets (LDs) and show altered content after ethanol administration: potential role in alcohol-impaired LD metabolism. *Alcohol Clin. Exp. Res.* **38**, 327–335 (2014).
- Turro, S. et al. Identification and characterization of associated with lipid droplet protein 1: A novel membrane-associated protein that resides on hepatic lipid droplets. *Traffic* **7**, 1254–1269 (2006).
- Li, C. & Yu, S. S. Rab proteins as regulators of lipid droplet formation and lipolysis. *Cell Biol. Int.* **40**, 1026–1032 (2016).
- Bersuker, K. et al. A proximity labeling strategy provides insights into the composition and dynamics of lipid droplet proteomes. *Dev. Cell* **44**, 97–112.e117 (2018).
- Gocz, P. M. & Freeman, D. A. Factors underlying the variability of lipid droplet fluorescence in MA-10 Leydig tumor cells. *Cytometry* **17**, 151–158 (1994).
- Greenspan, P., Mayer, E. P. & Fowler, S. D. Nile red: a selective fluorescent stain for intracellular lipid droplets. *J. Cell Biol.* **100**, 965–973 (1985).
- Brasaemle, D. L. et al. Adipose differentiation-related protein is an ubiquitously expressed lipid storage droplet-associated protein. *J. Lipid Res.* **38**, 2249–2263 (1997).
- Kassan, A. et al. Acyl-CoA synthetase 3 promotes lipid droplet biogenesis in ER microdomains. *J. Cell Biol.* **203**, 985–1001 (2013).
- Lu, Y. et al. Vacuolin-1 potently and reversibly inhibits autophagosome-lysosome fusion by activating RAB5A. *Autophagy* **10**, 1895–1905 (2014).
- Ye, Z. et al. Vacuolin-1 inhibits endosomal trafficking and metastasis via CapZbeta. *Oncogene* **40**, 1775–1791 (2021).
- Ye, Z. et al. Manipulation of PD-L1 endosomal trafficking promotes anticancer immunity. *Adv. Sci. (Weinh.)* **10**, e2206411 (2023).
- Chen, C. et al. Identification of novel vacuolin-1 analogues as autophagy inhibitors by virtual drug screening and chemical synthesis. *Molecules* **22**, 891 (2017).
- Song, J. et al. Identification of two pathways mediating protein targeting from ER to lipid droplets. *Nat. Cell Biol.* **24**, 1364–1377 (2022).
- Xu, D. et al. Rab18 promotes lipid droplet (LD) growth by tethering the ER to LDs through SNARE and NRZ interactions. *J. Cell Biol.* **217**, 975–995 (2018).
- Salo, V. T. et al. Seipin regulates ER-lipid droplet contacts and cargo delivery. *EMBO J.* **35**, 2699–2716 (2016).
- Itabe, H., Yamaguchi, T., Nimura, S. & Sasabe, N. Perilipins: a diversity of intracellular lipid droplet proteins. *Lipids Health Dis.* **16**, 83 (2017).
- Lytton, J., Westlin, M. & Hanley, M. R. Thapsigargin inhibits the sarcoplasmic or endoplasmic reticulum Ca-ATPase family of calcium pumps. *J. Biol. Chem.* **266**, 17067–17071 (1991).
- Li, S. et al. Intracellular alkalization induces cytosolic Ca<sup>2+</sup> increases by inhibiting sarco/endoplasmic reticulum Ca<sup>2+</sup>-ATPase (SERCA). *PLoS One* **7**, e31905 (2012).
- Salo, V. T. et al. Seipin facilitates triglyceride flow to lipid droplet and counteracts droplet ripening via endoplasmic reticulum contact. *Dev. Cell* **50**, 478–493.e479 (2019).
- Daemen, S., van Zandvoort, M., Parekh, S. H. & Hesselink, M. K. C. Microscopy tools for the investigation of intracellular lipid storage and dynamics. *Mol. Metab.* **5**, 153–163 (2016).
- Timmermans, F. J. & Otto, C. Contributed review: Review of integrated correlative light and electron microscopy. *Rev. Sci. Instrum.* **86**, 011501 (2015).



36. Nguyen, T. B. et al. DGAT1-dependent lipid droplet biogenesis protects mitochondrial function during starvation-induced autophagy. *Dev. Cell* **42**, 9–21.e25 (2017).
37. Shi, M. et al. Amino acids stimulate the endosome-to-Golgi trafficking through Regulator and small GTPase Arl5. *Nat. Commun.* **9**, 4987 (2018).
38. Chen, Y. et al. Amino acid starvation-induced LDLR trafficking accelerates lipoprotein endocytosis and LDL clearance. *EMBO Rep.* **23**, e53373 (2022).
39. Nakajima, S., Gotoh, M., Fukasawa, K., Murakami-Murofushi, K. & Kunugi, H. Oleic acid is a potent inducer for lipid droplet accumulation through its esterification to glycerol by diacylglycerol acyltransferase in primary cortical astrocytes. *Brain Res* **1725**, 146484 (2019).
40. Dechand, C. R. P. et al. Triacsin C reduces lipid droplet formation and induces mitochondrial biogenesis in primary rat hepatocytes. *J. Bioenerg. Biomembr.* **49**, 399–411 (2017).
41. Wilfling, F. et al. Triacylglycerol synthesis enzymes mediate lipid droplet growth by relocalizing from the ER to lipid droplets. *Dev. Cell* **24**, 384–399 (2013).
42. Olarte, M. J. et al. Determinants of endoplasmic reticulum-to-lipid droplet protein targeting. *Dev. Cell* **54**, 471–487.e477 (2020).
43. Goldstein, J. L. & Brown, M. S. The LDL pathway in human fibroblasts: a receptor-mediated mechanism for the regulation of cholesterol metabolism. *Curr. Top. Cell Regul.* **11**, 147–181 (1976).
44. Banta, L. M., Robinson, J. S., Klionsky, D. J. & Emr, S. D. Organelle assembly in yeast: Characterization of yeast mutants defective in vacuolar biogenesis and protein sorting. *J. Cell Biol.* **107**, 1369–1383 (1988).
45. van Weert, A. W., Dunn, K. W., Geuze, H. J., Maxfield, F. R. & Stoorvogel, W. Transport from late endosomes to lysosomes, but not sorting of integral membrane proteins in endosomes, depends on the vacuolar proton pump. *J. Cell Biol.* **130**, 821–834 (1995).
46. Yoshimori, T., Yamamoto, A., Moriyama, Y., Futai, M. & Tashiro, Y. Bafilomycin A1, a specific inhibitor of vacuolar-type H<sup>+</sup>-ATPase, inhibits acidification and protein degradation in lysosomes of cultured cells. *J. Biol. Chem.* **266**, 17707–17712 (1991).
47. Mauvezin, C. & Neufeld, T. P. Bafilomycin A1 disrupts autophagic flux by inhibiting both V-ATPase-dependent acidification and Ca-P60A/SERCA-dependent autophagosome-lysosome fusion. *Autophagy* **11**, 1437–1438 (2015).
48. Bohdanowicz, M., Balkin, D. M., De Camilli, P. & Grinstein, S. Recruitment of OCRL and Inpp5B to phagosomes by Rab5 and APPL1 depletes phosphoinositides and attenuates Akt signaling. *Mol. Biol. Cell* **23**, 176–187 (2012).
49. Sun, Q., Westphal, W., Wong, K. N., Tan, I. & Zhong, Q. Rubicon controls endosome maturation as a Rab7 effector. *Proc. Natl Acad. Sci. USA* **107**, 19338–19343 (2010).
50. Borchers, A. C., Langemeyer, L. & Ungermann, C. Who's in control? Principles of Rab GTPase activation in endolysosomal membrane trafficking and beyond. *J. Cell Biol.* **220**, e202105120 (2021).
51. Borchers, A. C. et al. Regulatory sites in the Mon1-Ccz1 complex control Rab5 to Rab7 transition and endosome maturation. *Proc. Natl Acad. Sci. USA* **120**, e2303750120 (2023).
52. Poteryaev, D., Datta, S., Ackema, K., Zerial, M. & Spang, A. Identification of the switch in early-to-late endosome transition. *Cell* **141**, 497–508 (2010).
53. Podinovskaia, M., Prescianotto-Baschong, C., Buser, D. P. & Spang, A. A novel live-cell imaging assay reveals regulation of endosome maturation. *Elife* **10**, e70982 (2021).
54. van den Boomen, D. J. H. et al. A trimeric Rab7 GEF controls NPC1-dependent lysosomal cholesterol export. *Nat. Commun.* **11**, 5559 (2020).
55. Singh, R. et al. Autophagy regulates lipid metabolism. *Nature* **458**, 1131–1135 (2009).
56. Weidberg, H., Shvets, E. & Elazar, Z. Lipophagy: selective catabolism designed for lipids. *Dev. Cell* **16**, 628–630 (2009).
57. Gordon, P. B. & Seglen, P. O. Prelysosomal convergence of autophagic and endocytic pathways. *Biochem Biophys. Res Commun.* **151**, 40–47 (1988).
58. Berg, T. O., Fengsrud, M., Stromhaug, P. E., Berg, T. & Seglen, P. O. Isolation and characterization of rat liver amphisomes. Evidence for fusion of autophagosomes with both early and late endosomes. *J. Biol. Chem.* **273**, 21883–21892 (1998).
59. Collier, J. J., Suomi, F., Olahova, M., McWilliams, T. G. & Taylor, R. W. Emerging roles of ATG7 in human health and disease. *EMBO Mol. Med* **13**, e14824 (2021).
60. Schott, M. B. et al. Lipid droplet size directs lipolysis and lipophagy catabolism in hepatocytes. *J. Cell Biol.* **218**, 3320–3335 (2019).
61. Zimmermann, R. et al. Fat mobilization in adipose tissue is promoted by adipose triglyceride lipase. *Science* **306**, 1383–1386 (2004).
62. Kaur, J. & Debnath, J. Autophagy at the crossroads of catabolism and anabolism. *Nat. Rev. Mol. Cell Biol.* **16**, 461–472 (2015).
63. Dugail, I. Lysosome/lipid droplet interplay in metabolic diseases. *Biochimie* **96**, 102–105 (2014).
64. Kaushik, S. & Cuervo, A. M. Degradation of lipid droplet-associated proteins by chaperone-mediated autophagy facilitates lipolysis. *Nat. Cell Biol.* **17**, 759–770 (2015).
65. Valm, A. M. et al. Applying systems-level spectral imaging and analysis to reveal the organelle interactome. *Nature* **546**, 162–167 (2017).
66. Naslavsky, N. & Caplan, S. The enigmatic endosome - sorting the ins and outs of endocytic trafficking. *J. Cell Sci.* **131**, jcs216499 (2018).
67. Cerny, J. et al. The small chemical vacuolin-1 inhibits Ca<sup>2+</sup>-dependent lysosomal exocytosis but not cell resealing. *EMBO Rep.* **5**, 883–888 (2004).
68. Huynh, C. & Andrews, N. W. The small chemical vacuolin-1 alters the morphology of lysosomes without inhibiting Ca<sup>2+</sup>-regulated exocytosis. *EMBO Rep.* **6**, 843–847 (2005).
69. Rink, J., Ghigo, E., Kalaidzidis, Y. & Zerial, M. Rab conversion as a mechanism of progression from early to late endosomes. *Cell* **122**, 735–749 (2005).
70. Rambold, A. S., Cohen, S. & Lippincott-Schwartz, J. Fatty acid trafficking in starved cells: regulation by lipid droplet lipolysis, autophagy, and mitochondrial fusion dynamics. *Dev. Cell* **32**, 678–692 (2015).
71. Mehlem, A., Hagberg, C. E., Muhl, L., Eriksson, U. & Falkevall, A. Imaging of neutral lipids by oil red O for analyzing the metabolic status in health and disease. *Nat. Protoc.* **8**, 1149–1154 (2013).
72. Fowler, S. D. & Greenspan, P. Application of Nile red, a fluorescent hydrophobic probe, for the detection of neutral lipid deposits in tissue sections: comparison with oil red O. *J. Histochem Cytochem* **33**, 833–836 (1985).
73. Spandl, J., White, D. J., Peychl, J. & Thiele, C. Live cell multicolor imaging of lipid droplets with a new dye, LD540. *Traffic* **10**, 1579–1584 (2009).
74. Beutner, G. L. et al. TCFH-NMI: Direct access to N-Acyl imidazoliums for challenging amide bond formations. *Org. Lett.* **20**, 4218–4222 (2018).

## Acknowledgements

We thank members of Yue lab for their advice on preparing this manuscript. This work was supported by NSFC (32070702), Kunshan Shuang Chuang Grant (kssc202302073), Suzhou Innovation and Entrepreneurship Leading Talent Program (ZXL2024337), ITF (MRP/064/21, GHP/097/20GD, and MHP/072/21), Hong Kong Research Grant Council (RGC) grant (11103620 and 11104422), and research grants from Shenzhen Science and Technology Innovation Committee (SGDX20201103093201010 and JCYJ20210324134007020). W.P. is supported in part through the Cornell-

City University of Hong Kong Joint PhD program. A.Y. is grateful for the generous support of Drs. John Babish and Paracelsian.

## Author contributions

J.Y. conceived the study. W.P. designed the experiments. W.P., S.C., J.M., W.W., N.L., J.X., W.G., and H.L. performed the experiments and analyzed the data. J.Y. and W.P. wrote the manuscript. K.C., L.Z., A.Y., and G.Z. edited the manuscript and supervised the project. All authors read and approved the final manuscript.

## Competing interests

The authors declare no competing interests.

## Additional information

**Supplementary information** The online version contains supplementary material available at <https://doi.org/10.1038/s41467-025-57038-8>.

**Correspondence** and requests for materials should be addressed to Guangyu Zhu or Jianbo Yue.

**Peer review information** *Nature Communications* thanks the anonymous reviewer(s) for their contribution to the peer review of this work. A peer review file is available.

**Reprints and permissions information** is available at <http://www.nature.com/reprints>

**Publisher's note** Springer Nature remains neutral with regard to jurisdictional claims in published maps and institutional affiliations.

**Open Access** This article is licensed under a Creative Commons Attribution-NonCommercial-NoDerivatives 4.0 International License, which permits any non-commercial use, sharing, distribution and reproduction in any medium or format, as long as you give appropriate credit to the original author(s) and the source, provide a link to the Creative Commons licence, and indicate if you modified the licensed material. You do not have permission under this licence to share adapted material derived from this article or parts of it. The images or other third party material in this article are included in the article's Creative Commons licence, unless indicated otherwise in a credit line to the material. If material is not included in the article's Creative Commons licence and your intended use is not permitted by statutory regulation or exceeds the permitted use, you will need to obtain permission directly from the copyright holder. To view a copy of this licence, visit <http://creativecommons.org/licenses/by-nc-nd/4.0/>.

© The Author(s) 2025